Final Report

Date of Report: *August 10, 2016*

Contract Number: *DTPH5614HCAP04L*

Prepared for: *Dr. James Merritt, DOT/PHMSA*

Project Title: *Optimized Diagnosis and Prognosis for Impingement Failure of PA and PE Piping Materials*

Prepared by: *University of Colorado-Denver, Arizona State University*

Contact Information: *Dr. Yiming Deng and Dr. Yongming Liu*

Project ending date: *August 10, 2016*

ABSTRACT

Pipeline infrastructure and its safety is critical for the recovering of U.S. economy and our standard of living. Statistics from U.S. Department of Transportation (DOT) and Gas Technology Institute (GTI) show the decline in use of steel and cast iron piping materials is significant in recent years and the increase in pipeline system size is largely due to plastic pipe installations. However, failure inevitably occurs in plastic piping materials and impingement failure is caused by high localized stress concentration combined with defects and inclusions. The object of this project is to fundamentally understand and characterize the failure modes and associated material behaviors for modern plastic piping materials. The proposed optimized diagnosis and prognosis approach is thoroughly investigated. The dominating PE materials (make up nearly 97% of current plastic pipes) and the emerging PA pipes that can operate at much higher pressures and be installed using existing PE tools and techniques are compared.

TABLE OF CONTENTS

LIST OF FIGURES

LIST OF TABLES

CHAPTER 1 INTRODUCTION

Polyethylene (PE) is a cost effective solution for a broad range of piping problem in a variety of industries. It has been tested and proven effective for above ground, surface, buried applications. High- density polyethylene pipe (HDPE) can carry portable water, wastewater, chemicals, and compressed gases. Polyethylene is strong, extremely tough and very durable. Since it is a plastic material, polyethylene does not rust, rot or corrode, this will lower the life cycle costs (LCC).

PA-11 is a material of choice for corrosion free, aggressive hydrocarbon transport system. PA-11 thermoplastic material has been used across the entire oil and gas value chain extensively, for cost-effective non-metallic piping systems. PA-11 provides a better value compare to steel pipe. It has lower total installation cost, lower lifetime maintenance, and comparable performance. According to a brochure from Arkema, PA-11 also shows excellent resistance to slow crack growth.

The overall objectives of the proposed research are two-fold: optimized diagnosis-find existing impingement damage at the earliest stage before it becomes failure critical in PE and PA materials, conduct comprehensive comparison studies to identify the differences in cracking and failure behaviors between these two materials; and optimized prognosis - accurately predict the remaining strength and RUL of PE and PA components through mechanical modeling and experimental investigations.

CU Denver focuses on the sensing physics modeling of impingement failure diagnosis and experimental investigation assisted by model-based inversion techniques. Three subtasks are proposed in the paper. Chapter 2 proposed model-based inversion for ultra-fast impingement failure reconstruction and sensing assisted by compressed sensing techniques; Chapter 3 proposed element-free Galerkin's method (EFG) development for the electromagnetic modeling of arbitrary and micro-scale crack initiation and propagation due to impingement; Chapter 4 proposed Imaging optimization and comparison with DIC results.

ASU focuses on the experimental testing and numerical simulations of failure for PA and PE materials. Chapter 5 discusses the experimental testing procedures and results. It also contains the

testing results for specimens that are used for CU Denver diagnosis for comparison of surface strain measurements and microwave detections imaging. Experimental design for the investigation of surface defect size and depth are proposed and results are discussed with respect to two different material systems. Chapter 6 proposed a numerical simulation framework using extended finite element method (XFEM) and cohesive zone model (CZM). Detailed calibration procedure and validation examples are given. The difference of mechanical response for PA and PE material is discussed based on the experimental and numerical studies.

CHAPTER 2 SENSING PHYSICS MODELING OF IMPINGEMENT FAILURE DIAGNOSIS

PA-11 and PA-12 materials with impingement type damage are emphasized for this funded research. The critical component of the proposed sensing system, near-field microwave simulation and its interaction with plastic materials have been modeled using numerical methods. The preliminary impingement damage reconstruction results were shown in Figure 2.1. However, conventional model-based defects reconstruction is very time-consuming and computationally expensive. An innovative impingement defective pipe geometry reconstruction algorithm is being investigated to address this challenge by strategically reducing the number of measurements assisted by the concept of compressed sensing. CS-based imaging speed improvement experimentally has also been studied and discussed.

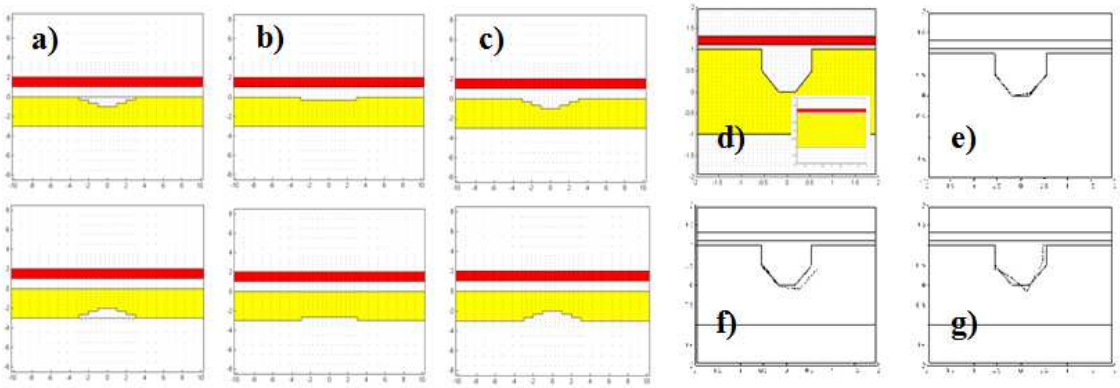

Figure 2.1Impingement OD and ID defects reconstruction using state-space search method

(Left): (a) true profile, (b) initial guess and (c) reconstructed profile and deeper OD defects reconstruction; using gradient search method

(Right): (d) true profile and initial guess and reconstructed profiles with (e) 5% measurement noise, (f) 15% measurement noise and (g) 25% measurement noise

A 3D simulation study was simultaneously conducted using FEKO software and the simulation geometry is shown in Figure 2.2 for an antenna array sensor. Preliminary physical modeling result is shown in Figure 2.3. Further investigation will continue in the next quarter.

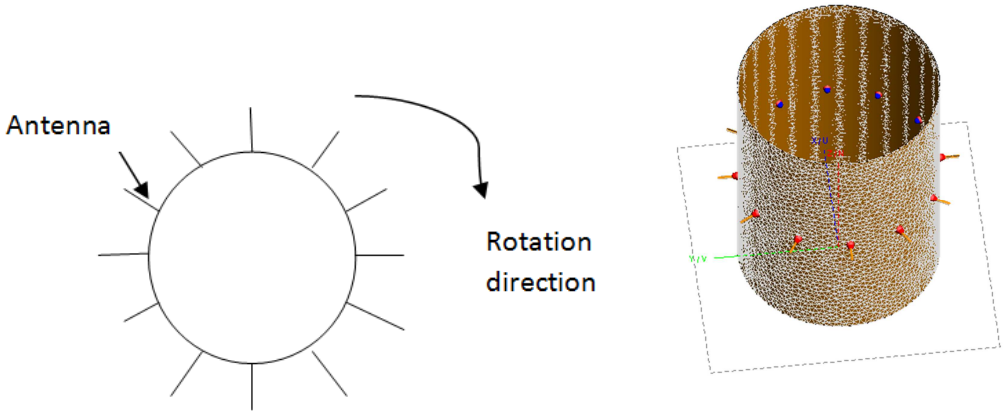

Figure 2.2 3D simulation for the NFMW imaging system with array geometry

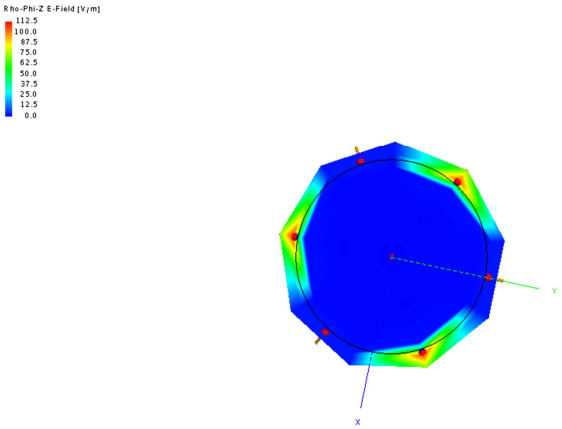

Figure 2.3 Three channel NFMW imaging sensors with radiation pattern for pipe sections without impingment damage.

2.1. Physics modeling for imaging of PE and PA piping materials

Polyethylene(PE) is a cost effective solution for a broad range of piping problem in a variety of industries. It has been tested and proven effective for above ground, surface, buried applications. High- density polyethylene pipe (HDPE) can carry portable water, wastewater, chemicals, and compressed gases. Polyethylene is strong, extremely tough and very durable. Since it is a plastic material, polyethylene does not rust, rot or corrode, this will lower the life cycle costs.

PA11 is a material of choice for corrosion free, aggressive hydrocarbon transport system. PA11 thermoplastic material has been used across the entire oil and gas value chain extensively, for cost-effective non-metallic piping systems. PA11 provide a better value compare to steel pipe.

It has lower total installation cost, lower lifetime maintenance, and comparable performance. According to a brochure from ARKEMA, PA11 also shows excellent resistance to slow crack growth.

Simulation study is an important way to assist experimental studies and sensor development via optimization of critical parameters. In this quarter, we developed a FEKO model to assist the experiment scanning. The goal of the simulation is to study the electric field distribution along the target to verify the experiment results. The scanning probe is designed as a monopole antenna in the simulation which is mounted on an infinite perfectly electric conducting ground. We chose infinite PEC ground to avoid the reflection due to the size of ground plane. The cutoff frequency of the probe tip set at 3GHz, the size of the monopole antenna is quarter of wavelength, which is 2.5cm. First, we design a PA material with size of 13.375in x 19.125in x 0.313in, a hole with a radius of 5mm is introduced at the center of the target. Since the size of the probe tip is 2mm, this will help us identify the resolution of the scanning probe. Fig 2.4(a) below shows the design of the simulation. We move probe tip along x direction to see if the probe tip is able to detect the whole at the center.

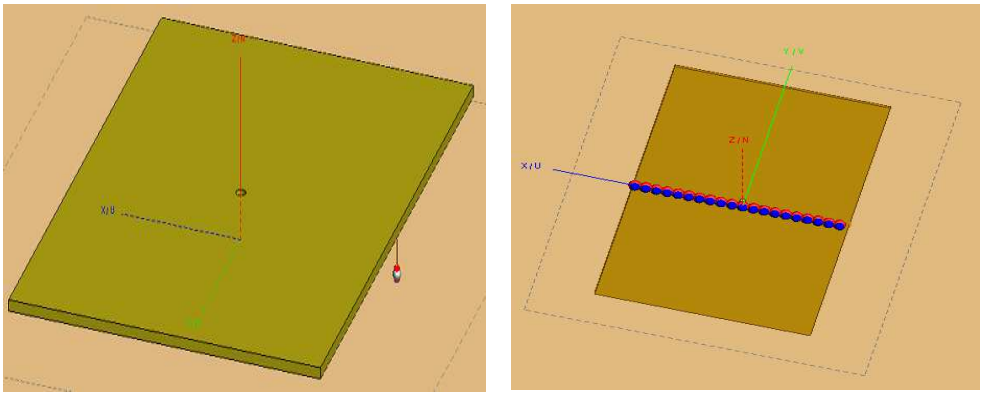

(a) (b)

Figure 2.4 Simulation geometry of the PA material

Due to the processing speed of the computer, we put 20 probe tip along x direction at the center of the sample as shown in Fig. 2.4(b). This will reduce the simulation time. Fig.2 shows the simulation result along both x and y direction. From Fig. 2.5 we can clear see that there is a whole right at the center of the target from both x and y direction. The ripples that show in the results are due to the radiation between each scanning probe tip. The distance between each probe tip is

17mm, which is less than one wavelength, this will introduce noise to the results. Even with the noise we have, we can still clear see the hole from the center, this gave us the confident that the size of the probe tip is good enough to achieve high resolution images.

Next, we design a simulation for PE material. The size of the sample is 18in x 12in x 0.4in. Several defects have been introduced to the sample as the experiment setup to verify the experiment results. As shown in Fig. 2.6, we introduced different sizes of square to the sample. The depth of the square is 0.236in, which is thinner than the sample. The length of the sides of each square is 3in, 2in, 1.5in and 1in. We locate the probe tip on the smooth side of the sample, to see if we are able to detect the defects. We move probe tip only along y-axis, the simulation results should be able to show the different size of squares.

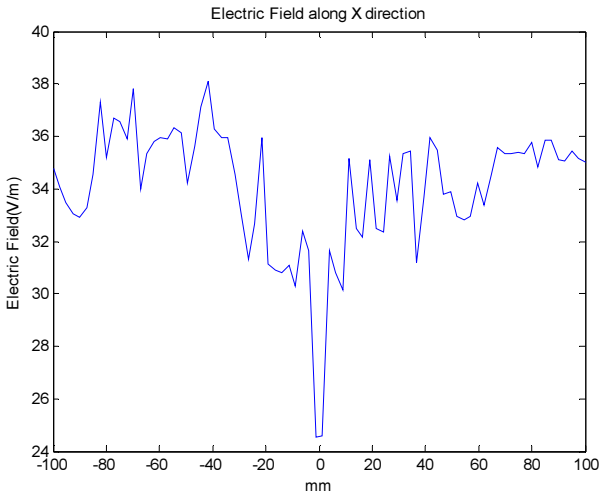

(a)

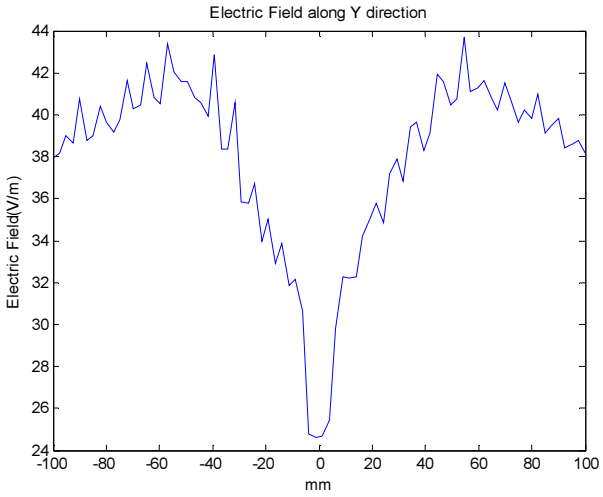

(b)

Figure 2.5 simulation result along both x and y direction

(a) Electric field achieved from X direction. (b) Electric field achieved from Y direction

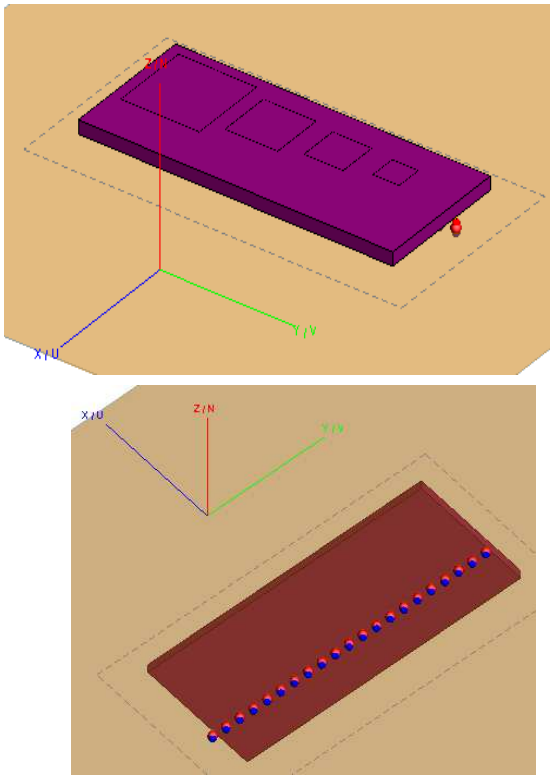

Figure 2.6 Simulation geometry of the PA material

Fig. 2.7 shows the result of the PE material simulation. From the results we can clear see the four squares along y-axis. Since we put the probe tip at the smooth side, this proof the

capability of the probe tip for penetrating the material and also able to detect the defect. The ripples in the Fig.4(b) also caused by the close distance between each probe tip. To improve the simulation design and also develop the algorithm for meshless model will implement during the next quarter.

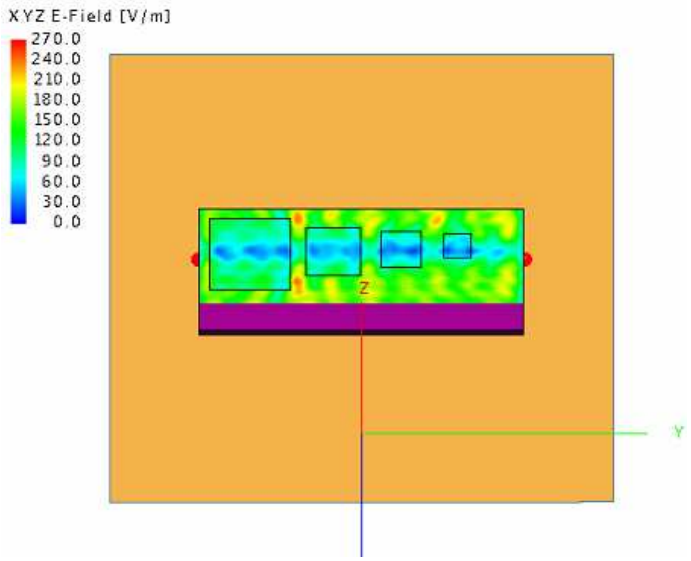

(a)

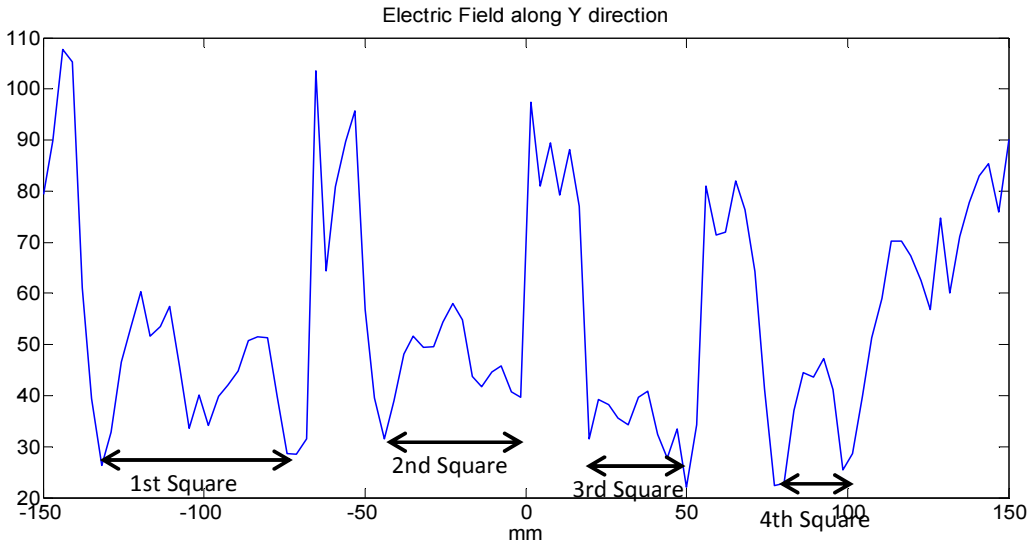

(b)

Figure 2.7 Simulation results for PE material

The results showed that the size of the probes that we used in experiment have the abilities to

achieve high resolution images. We then studied PE and PA11 material properties using the model simulation results. For the experiment, the focus was to retrieve amplitude and phase of the reflected microwave to map the physical properties of the surface and subsurface of the material. The simulation model will focus on the radiation field of each scanning probe tips to verify if the scanning array has the ability to identify the different materials.

First, we compared the electric field of PA and PE material with circular pipe shaped antenna array. The design of the array showed in Fig. 2.8. The scanning array is formed by a metal cylindrical with 6 monopole antennas located inside of the pipe. The outer cylindrical is the pipe, which used PA and PE for comparison. The relative dielectric constant for PA and PE is 3.4 and 2.25 respectively. Since PA has slightly higher dielectric constant value compare to PE material, we expect to see that PE material has higher electric field around the probe tips than PA material. Because the simulation results showed the field that radiated around the tip. The higher dielectric constant means the material stores more energy and more response with same shape and voltage. PA material should have more reflection compare to PE material, which means PE material will have more field concentrated around the probe tip than PA material.

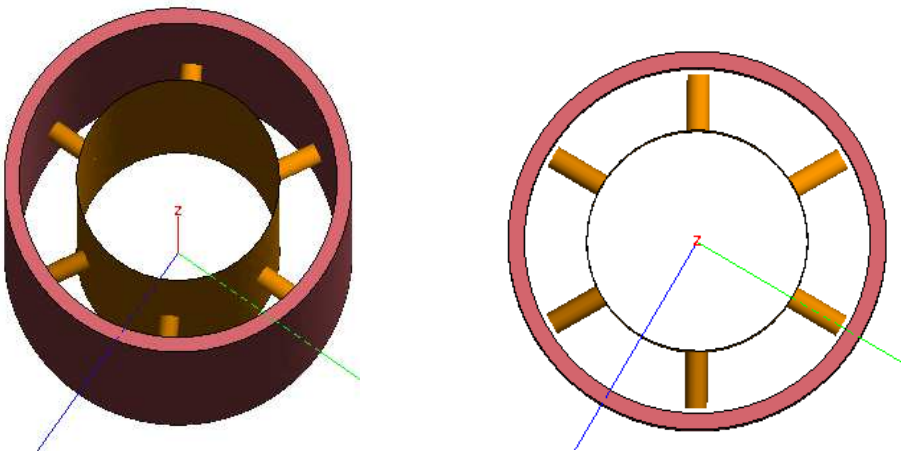

Figure 2.8 Circular pipe shaped scanning array

Fig. 2.9 shows the simulation results of PA and PE material with circular pipe shaped scanning array. As expected, electric field for PA is lower than for PE. This can help us to identify the materials during the experiment.

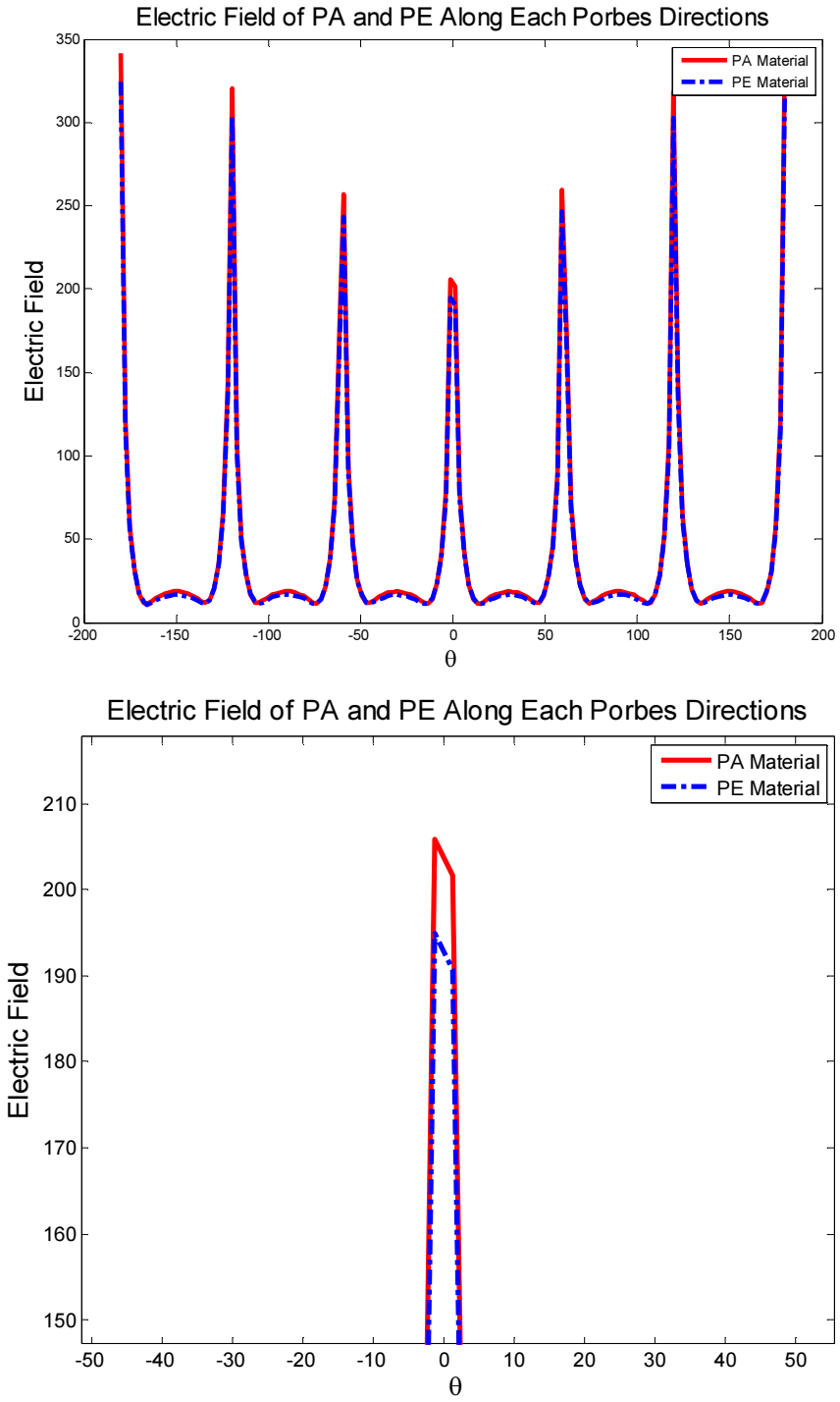

Figure 2.9 Comparison of near-field microwave responses for PE and PA11 materials.

we further studied PE and PA11 material properties using 3D models with 1D linear array and 2D scanning array. For the experiment, the focus was to retrieve amplitude and phase of the reflected microwave to map the physical properties of the surface and subsurface of the material, then compare

with the digital image correlation (DIC) results obtained at ASU team. The simulation model will focus on the radiation field of each scanning probe tips to verify if the scanning array has the ability to identify the different materials.

First, we compared the electric field of PA and PE materials with linear array in a validated 3D model developed in Q1 to Q4. The design of the array showed in Fig. 1. The diameter of the hole or artificial damage is 5 mm. Both PE and PA plate have the same size of 340 mm x 486 mm x 8 mm, which is the same as the actually testing sample in the CU LEAP lab. We further validated the conclusion we reached at the end of Q4 that since PA has slightly higher dielectric constant value compare to PE material, we expect to see that PE material has higher electric field around the probe tips than PA material. Because the simulation results showed the field that radiated around the tip. The higher dielectric constant means the material stores more energy and more response with same shape and voltage. PA material should have more reflection compare to PE material, which means PE material will have more field concentrated around the probe tip than PA material.

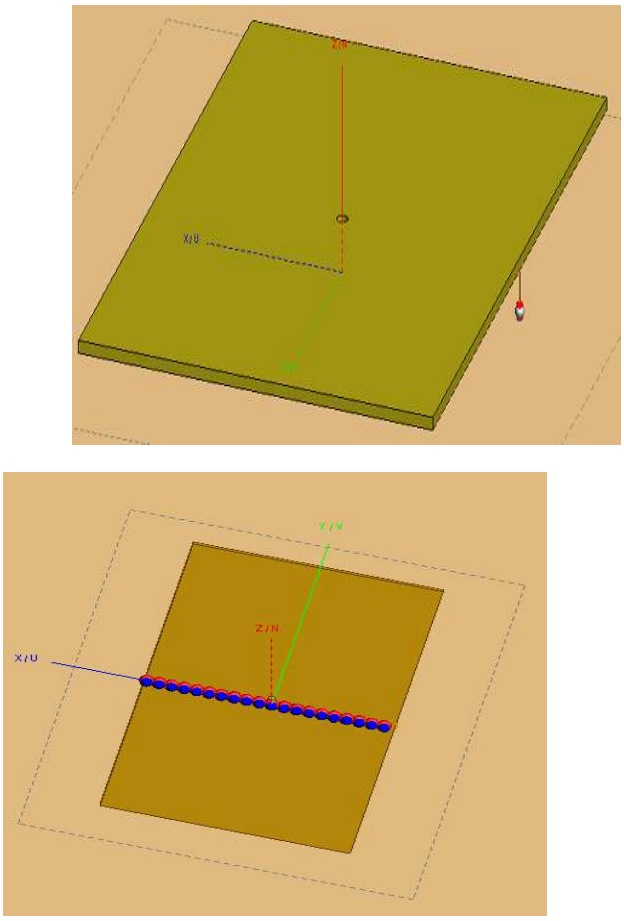

Figure 2.10 Linear scanning array for both PE and PA plate model

Fig. 2.11 shows the simulation results of PA and PE material with circular pipe shaped scanning array. As expected, electric field for PA is lower than for PE. This can help us to identify the materials during the experiment.

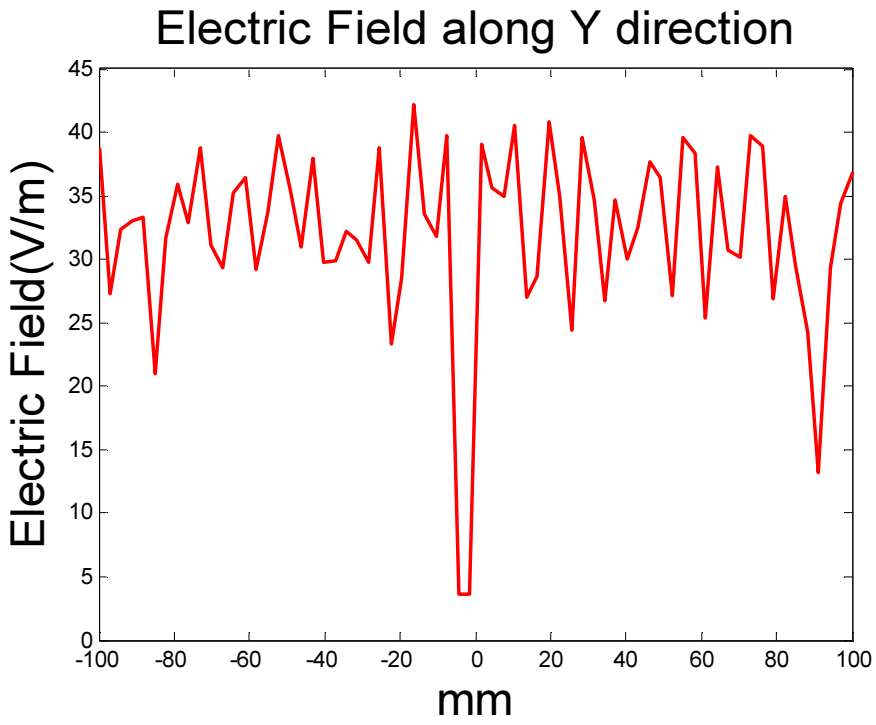

(a)

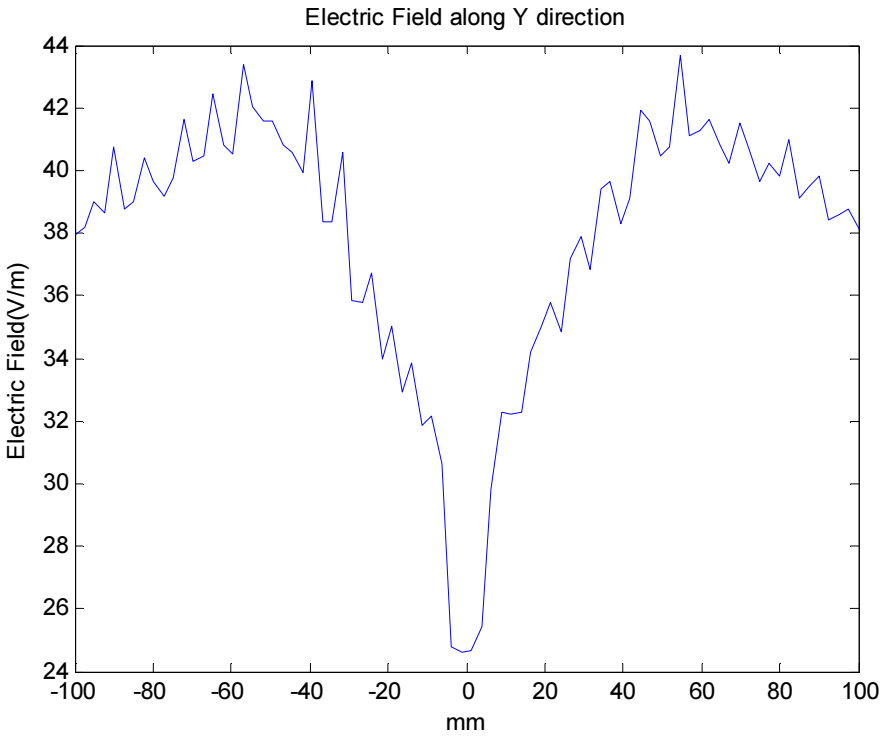

(b)

Figure 2.11 Comparison of near-field microwave responses of single hole damage and linear

scanning array

for (a) PE and (b) PA-11 materials. Larger signal (E-field intensity) is expected from PA-11 sample.

Next, a two-dimensional (2D) scan is simulated in this well-developed 3D model and the exemplary imaging result is shown in Fig. 2.12. Subsurface square damage are clearly identified and segmented from the image data, which demonstrated the detection capability of the developed sensor array for PE and PA materials. The extracted 1D signals are shown in Fig. 2.13, in which the PA materials had higher damage responses than PE materials, which means that the damage will be more sensitive or easier to be detected for PA using the same diagnosis technique developed under this project.

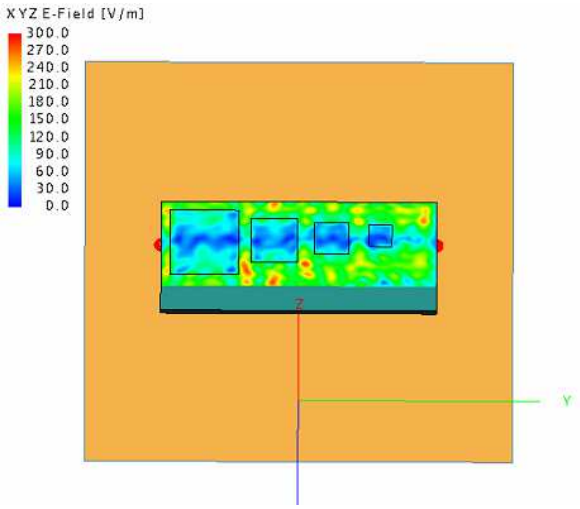

Figure 2.12 2D imaging results for damage detection of PA-11 sample.

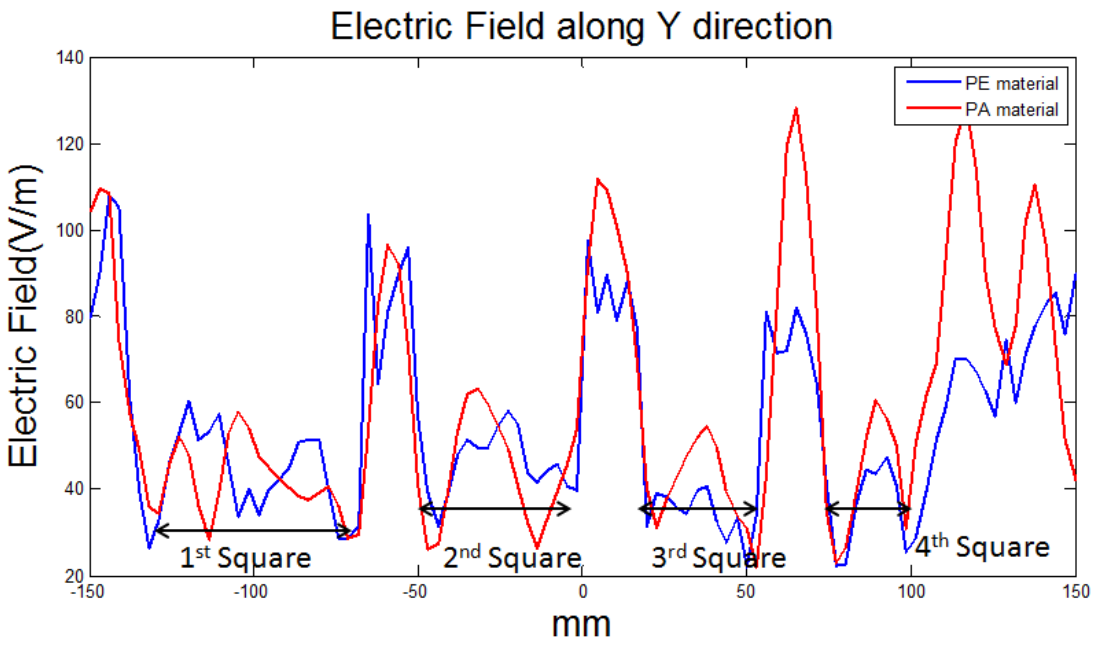

Figure 2.13 Comparison of 1D PE and PA materials responses to square damage with different sizes.

2.2. Multichannel scanning sensor model development for PE and PA materials

we introduced a preliminary model for a multichannel scanning sensor at the beginning of this project. The sensor was design as pipe shaped tube with scanning probes mounted outside. The goal is to move the sensor along within the pipe to collect data from the inside of the pipe.

We then redesign the scanning sensor system. In quarter 1, we used a pipe shaped tube as scanning sensor, the tube served as ground plane for each scanning probe. But since it is a cylinder, the ground plane is not perfectly perpendicular to the probes, which may cause reflection from the ground plane. So we design a cubic shaped scanning sensor first to verify the reflection and coupling in the system.

Fig. 1 shows the geometry of the cubic sensor. The size of the cubic is 10cm x 10cm x 10cm, which is smaller than the diameter of the pipe (15cm). The radiating frequency of the scanning probe is at 3GHz, the length of the probe is 2.5cm. The scanning probes are located at the center of each sides of the cubic. This design would make sure the each probe is perpendicular to the ground plane and will maximize the power radiating from the probes.

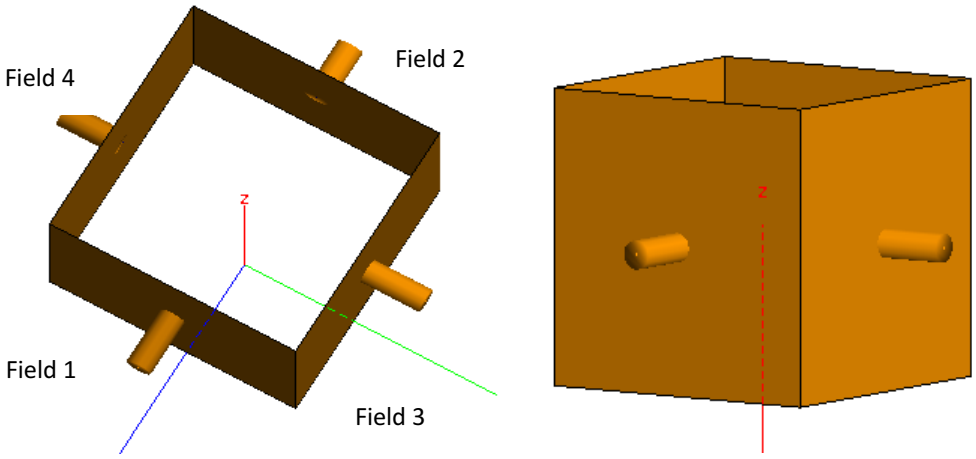

Figure 2.14 Geometry of a cubic multi channel scanning sensor

To verify the design, we need to look at the following parameters: reflection coefficient, VSWR, electric field. Reflection coefficient will give us an idea about how well the antenna works for the system, same as VSWR. Electric field will show us if the field around each antenna is symmetric or not.

According to the simulation result, the reflection coefficient of each probe is only 6%, which means most of the power is transmitted to the air and there is barely any reflection in the system. Same as VSWR, the value of VSWR for each antenna is close to 2. Next we are going to look at the electric field value to verify if the probes are radiating equally. Fig.2.15 shows the electric field plot for each probe.

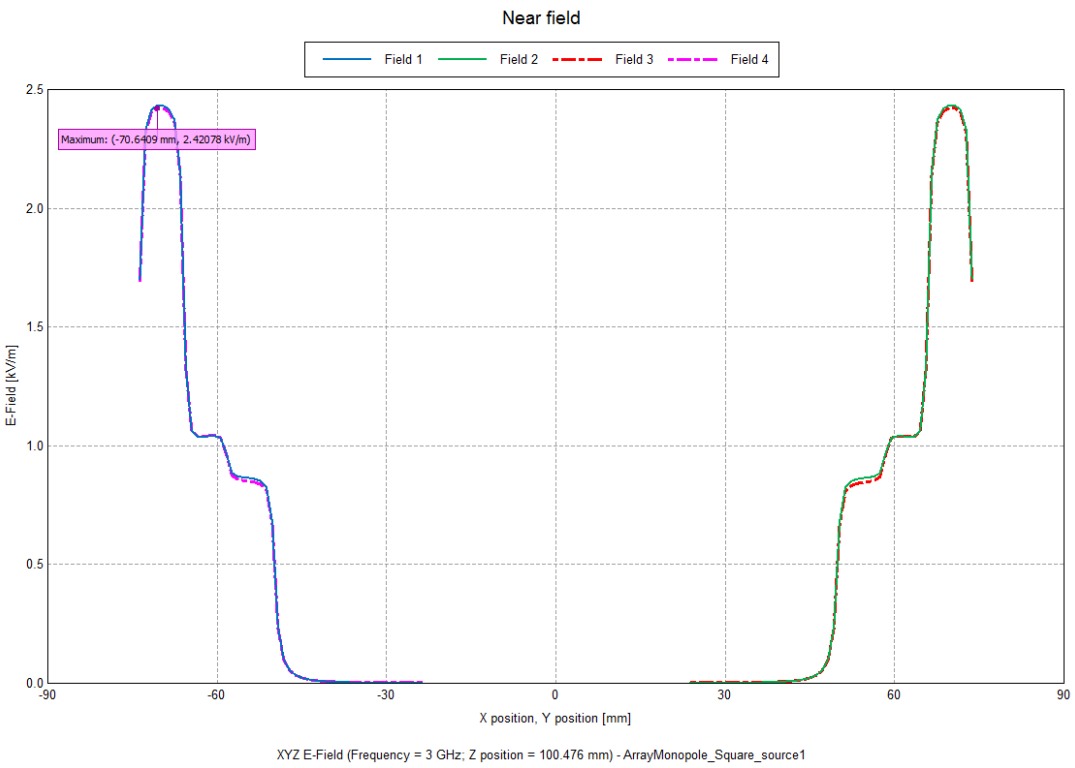

Figure 2.15 Electric field of each scanning probe along probe direction

The electric field in Fig. 2.15 shows that the electric field along probe direction is symmetric and radiating equally in the air. This gave us a promising result for future development.

Next we add a PE pipe material on the outside of the scanning sensor. The geometry showed in Fig. 2.16. The diameter of the pipe is 15cm, the pipe will be a couple millimeters away from the scanning probe tip. The permittivity of PE material is 2.26, loss tangent is 0.00031. The goal for this simulation is to verify if the reflection coefficient increases compare to the previous simulation. Since we feed each probe using the same voltage source, both reflection coefficient and VSWR should show a similar value among all of the probes. Our goal is to have as high as possible reflection coefficient and VSWR, so we can measure the reflection signal from the target. According to the simulation result, the reflection coefficient has been increased to 14.25%, which means there are more signal has been reflected back from the target compare to the air.

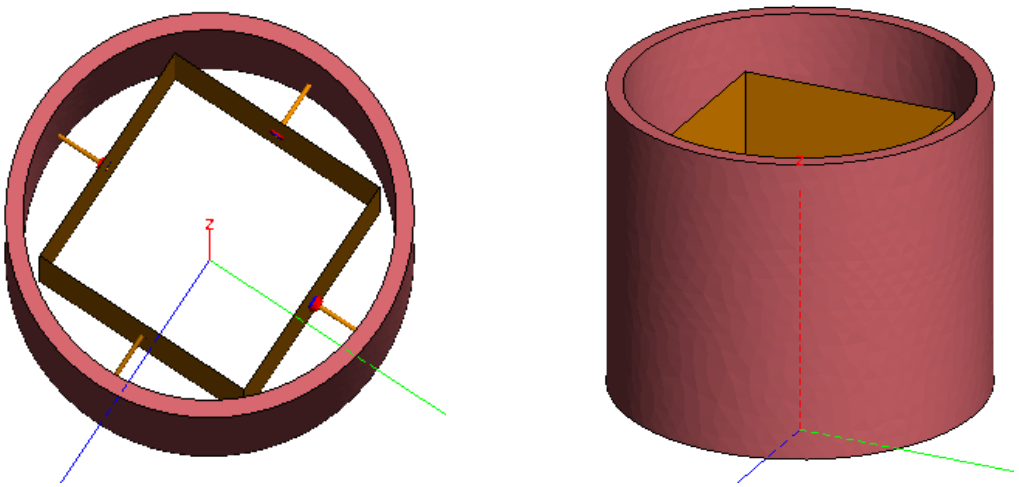

Figure 2.16 Geometry of a cubic multi channel scanning sensor with pipe

We also compared the electric field of each probe along the probe direction shown in Fig. 2.17. From Fig. 2.17 we can see that the field still symmetric and radiating equally, which same as the simulation in the air. The only difference we have is the maximum value of the electric field. Fig. 2.17 shows how much field radiated from each probe. Due to the reflection from the target, the field around the probe is lower than the one without the target.

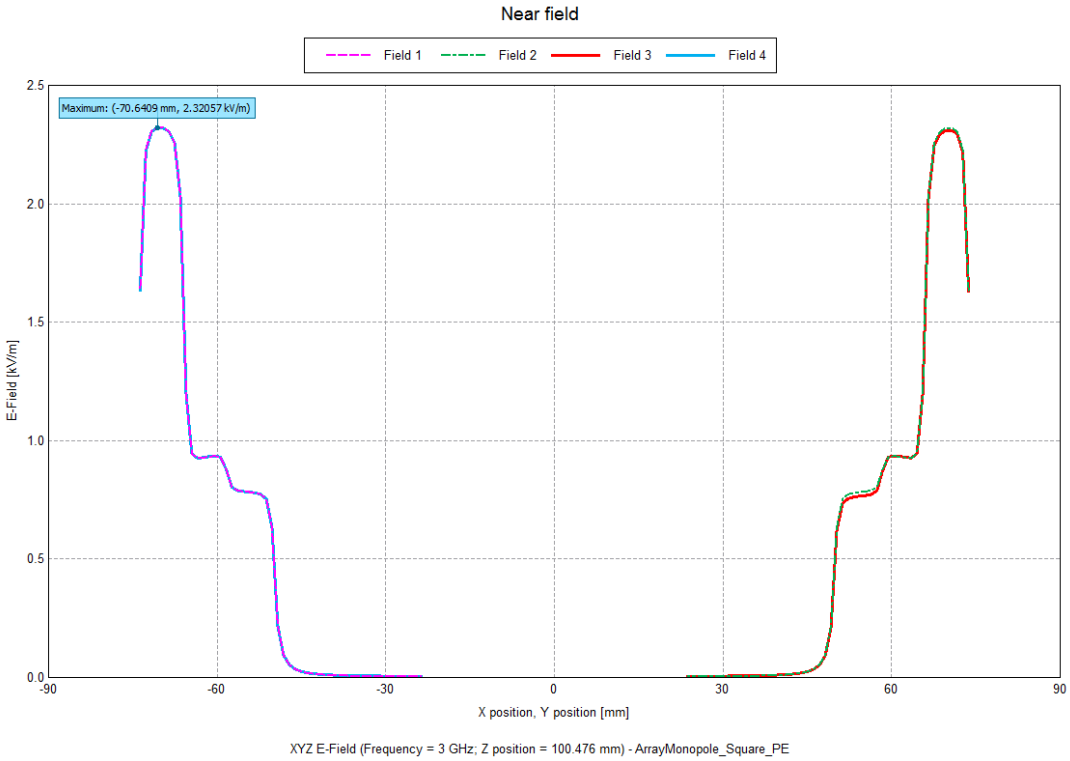

Figure 2.17 Electric field of each scanning probe along probe direction with target

Meanwhile, the multi-channel sensing prototype is being developed. In this 5th quarter, we designed and fabricated the multi-channel scanning sensor tip the control circuit for the multi-channel scanning sensor for improving the scanning speed. A control circuit also has been designed same setup as the current experiment. The innovative design of the control circuit shows in Fig. 2.18(a). Compared with the current experiment, shown in Fig. 2.18(b), the control circuit compresses the directional coupler, RF to AC converter and data collection together to perform the same function. The control circuit uses a microcontroller to control the input and receive signal. There is no connection between data processing and receiving signal in the control circuit design, which will reduce the scanning time.

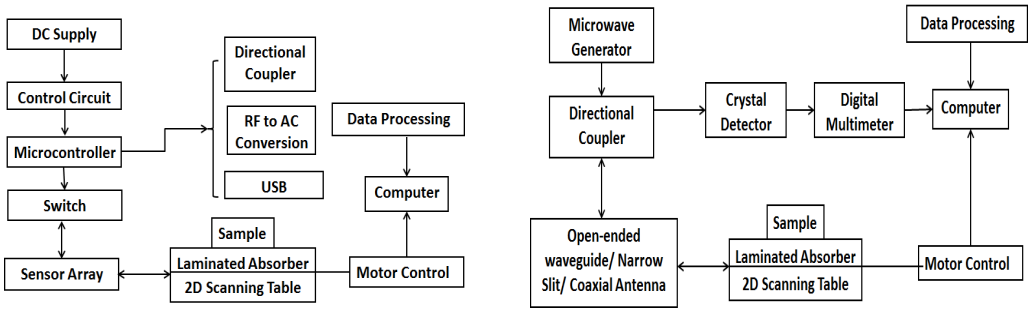

(a) Improved design with Control circuit (b) Current experiment design

Figure 2.18 Design comparison of control circuit and current experiment setup

CHAPTER 3 ELEMENT-FREE GALERKIN'S METHOD DEVELOPMENT

3.1. Background

Finite element method is a very general and powerful numerical method for solving the boundary value problem. One drawback of this method is the heavy workload of the data preparation which due to the meshing calculation, especially for the complicated three-dimensional problem. When simulating plastic materials which might have crack propagation or large deformations, it would be hard to maintain the connectivity of the mesh and result in error output. Therefore, remeshing is usually needed and leading to high computational cost. Many difficulties associated with Finite element method have been solved by the element-free Galerkin (EFG) method. As a new type of numerical methods, meshless method is no longer depending on the concept of element. This type of methods avoid the heavy workload of mesh generation and element distortion.

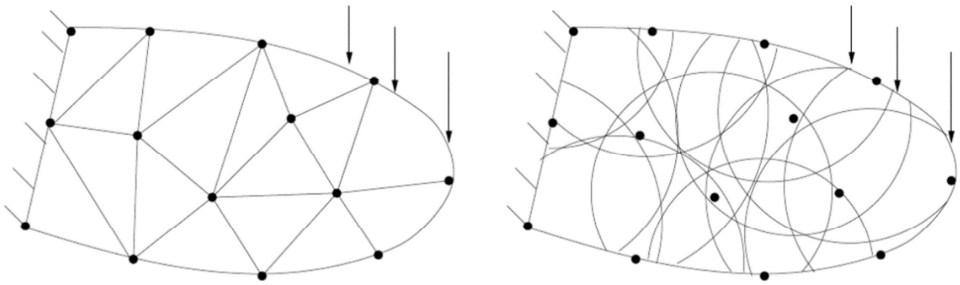

Finite element method Element-free Galerkin method

Figure 3.1 Nodes in mesh and meshless method

3.2. Moving Least Square Method:

Moving least square is a meshless way to approximate functions. If the Approximate expression of an Unknown field function $u^h(x)$ can be Simulate as:

$$u^h(x) = \sum_{j=1}^{m} p_j(x) a_j \equiv P^T(x) a(x)$$

Where m represent the dimension of basis function. P(x) is the polynomial basis vector.

$$P(x) = [p_1(x),....,P_j(x)...,p_m(x)]^T$$

For Two dimensional linear basis: $P(x) = [1, x, y]^T$

For Two dimensional quadratic linear basis: $P(x) = [1, x, y, x^2, xy, y^2]^T$

a(x) is the Global coefficient vector, which is:

$$\mathrm{a}(\mathrm{x}) = [\mathrm{a}_1(x), a_2(x),....a_m(x)]^T$$

In order to solve the value of a(x), MLS try to find the minimum value of:

$$J(x) = \sum_{I=1}^{N} W(x - x_1)[P^T(x_I)a(x) - u_I]^2$$

W(x) is the weight function. The weight function has a great influence on the result of least squares fitting. Selection generally follows the following rules:

(1) The weight function remains non negative under any circumstances;

(2) The weight function of compact support domain should ensure the existence and uniqueness of A - 1 (x);

(3) The points at the different distance to the fitting point have different influence.

3.3. Accuracy analysis of the Moving Least Square Method

When using moving least square method to find the function approximation by establishing the shape function and solve the numerical solution for partial differential equations. The reasonable establishment of the shape function directly determines the accuracy of function approximation and numerical results.

The rational establishment of the shape function is determined by the following three aspects:

(1) the selection of weight function

(2) the order of basis functions;

(3) domain of influence of each node

In order to study the influence of the order of the basis functions and the influence of nodes on the function approximation and the numerical solution precision. Gauss weight function

is selected as the weight function. Several pairs of basis functions and node's domain of influence have been evaluate in order to find the general rule of the reasonable establishment of the shape function. The approximation function is f(x) = x*sin(x) with length 10.

Figures below are the comparisons between the approximation function and the reference function. In each figure, the original function, the first order derivative and the second order derivative are shown from top to bottom, respectively. The blue line is the reference function, and the red line is the approximation function.

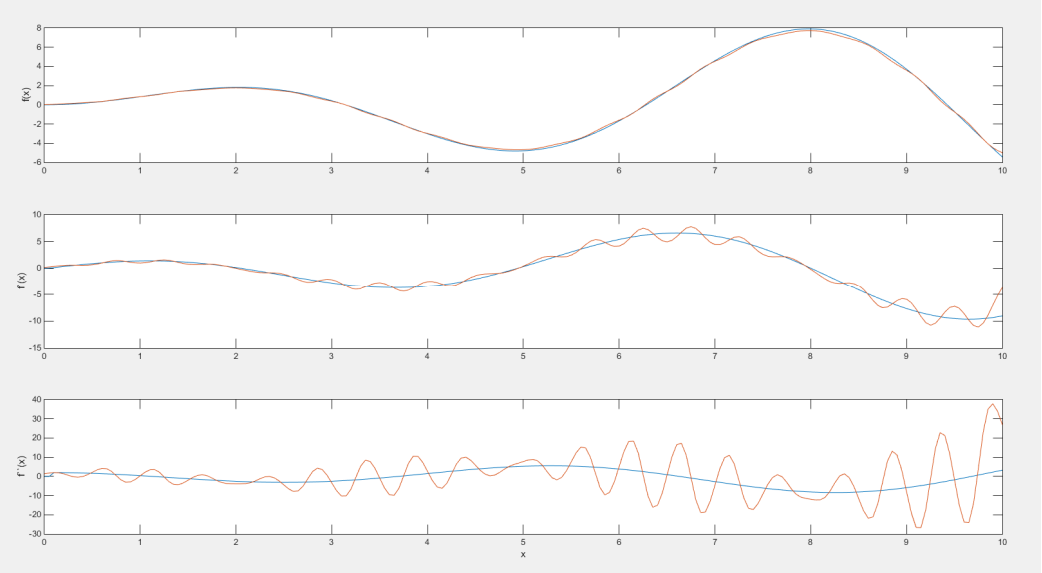

Fig.6 Constant basis with nodes' Radius of support equal to 2

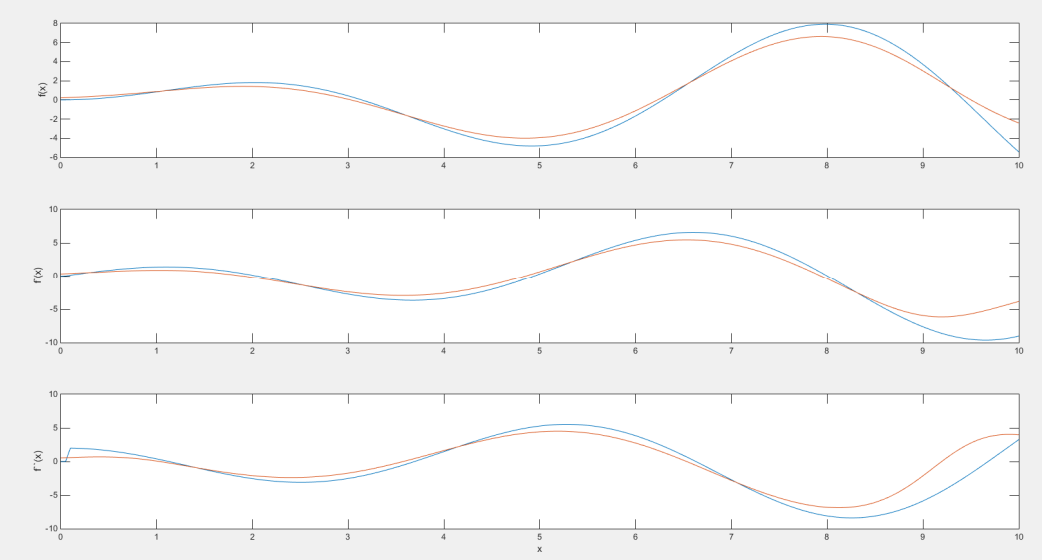

Fig.7 Constant basis with nodes' Radius of support equal to 5

As figures shown above, for a constant basis function, the errors of fitting function and the derivative of each order is large with a small influence domain of each node. The numerical oscillations disappear when the domain of influence of nodes are increased. However, the approximation results still have large errors. This might due to the constant basis function gives low order shape function, which resulting in a big approximation error of higher order function simulation.

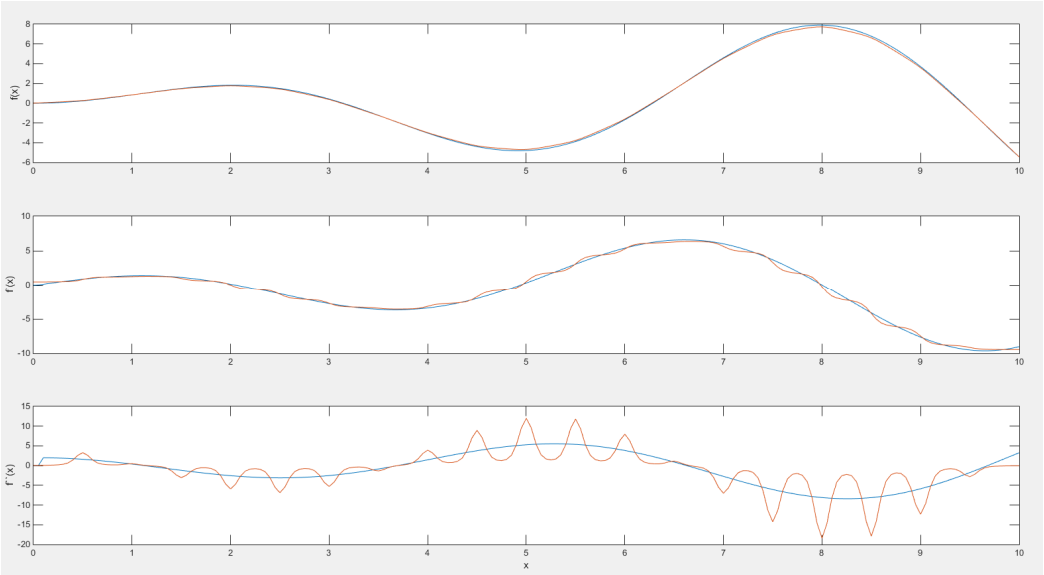

Fig.8 Linear basis with nodes' Radius of support equal to 2

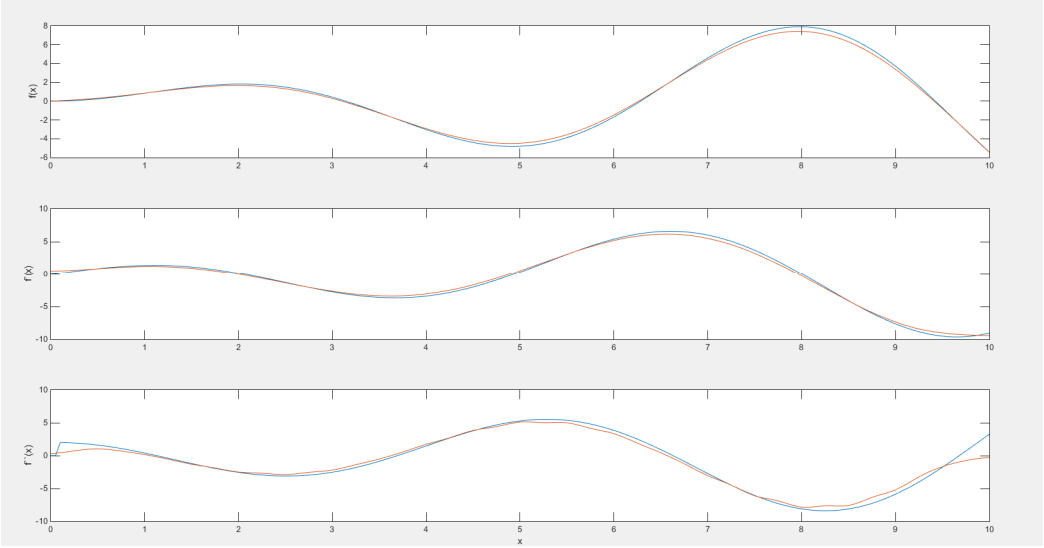

Fig.9 Linear basis with nodes' Radius of support equal to 5

As figure shown above, a better performance is given when applying the linear basis function. Approximation function can obtain better accuracy as the domain of influence of nodes increase. Figure below shows that quadratic basis function resulting in a huge error with low nodes' support radius. Numerical oscillations vanish when approaching a higher nodes' support radius, the error of first derivative and the second derivative is still larger than the result of linear basis function.

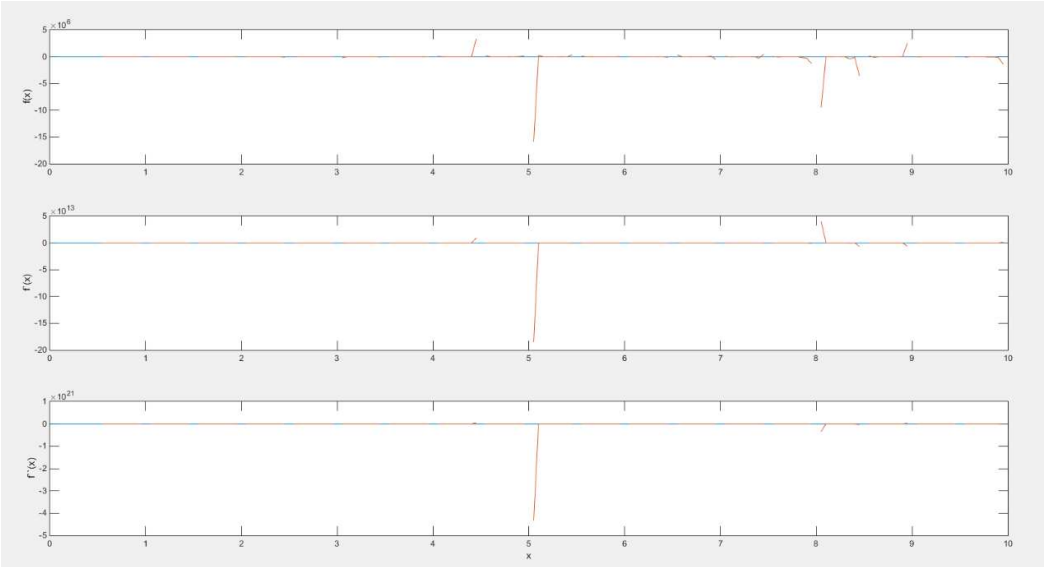

Fig.10 Quadratic basis with nodes' Radius of support equal to 2

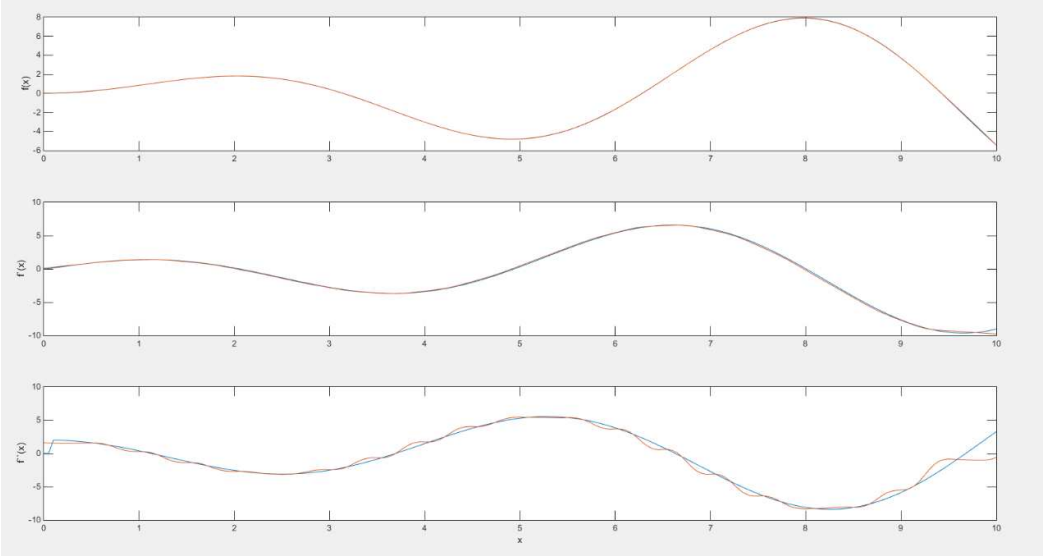

Fig.11 Quadratic basis with nodes' Radius of support equal to 5

Therefore, the approximation accuracy can be determined by using the appropriate basis functions and the number of fitting nodes within the influence region. Using the high order polynomial function as the basis function to construct the shape function, it may lead to numerical oscillation instead of improve the accuracy.

3.4. Development of Element-free Galerkin (EFG) Method for impingement damage imaging

Based on moving least square approximations, the EFG is a powerful numerical method which uses only a set of nodal points and a boundary description to formulate the discrete model. In order to find the approximation from discrete nodes, MLS trying to find minimum value of

$$\mathrm{J(x)} = \sum_{i=1}^{n} w(x - x_i)[p^T(x_i)\alpha(x)$$

Which can be minimized by setting the derivative of with respect to equal to zero

$$\frac{\partial \mathrm{J}}{\partial \alpha} = 0 \quad \ll=\gg \quad \sum_{i=1}^{n} w(x - x_i)2p_i(x)[p^T(x_i)\alpha(x) - u_i]^{\,2}$$

Therefore, we can get $\alpha(\mathrm{x})$ with:

$$with \;\; A(\mathrm{x}) = \sum_{i=1}^{n} w(x$$

$$and \quad B(\mathrm{x}) = \sum_{i=1}^{n} w(x$$

The weight function plays a very important role in the process of building the shape function. The introduction of weight function makes the approximation function has the property that the approximate value of any single point is only affected by serval neighbor nodes, and the nodes outside the influence range will not affect the approximate value of the point. In this simulation, we use negative exponential weight function:

$$w(s) = \begin{cases} c_1 \dfrac{e^{-(c_2 s)^2} - e^{-(c_2)^2}}{1 - e^{-(c_2)^2}}, s \le 1 \\ 0 \qquad\qquad\qquad\quad , s > 1 \end{cases}$$

C1 will influence the magnitude of the weight function, and C2 can be used to adjust the image shape of the weight function.

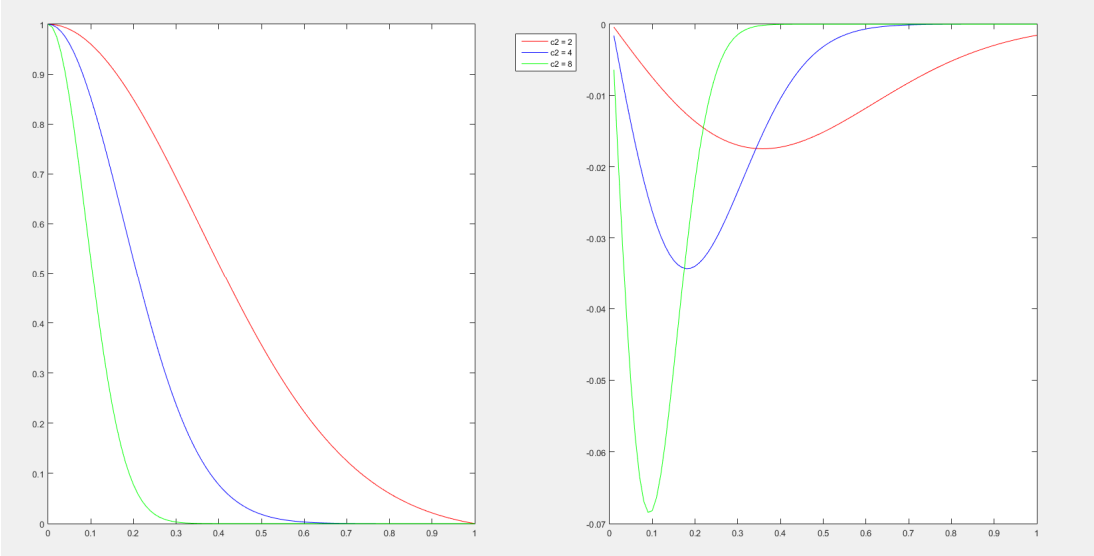

Figure 3.2 Graphs of weight functions and their derived functions.

Coefficients of the weight function are adjusted in order to improve the calculation accuracy. The derived function with respect to S is

$$\frac{d}{ds} w(s) = -\frac{e^{-(c_2 s)^2}}{1 - e^{-(c_2)^2}} 2(c_2)^2 s$$

Therefore, we can calculate the weight of any points to the nodes within the domain.

3.5. Methodology

Assume an electromagnetic field constitute of a single medium. L_1 represents for the left boundary and the rest of the boundary is represented by L_2. The permeability of the medium is μ. A_z is the vertical vector magnetic potential. Therefore, its mathematical model can be expressed as:

$$\begin{cases} \Omega: \frac{1}{\mu}\nabla^2 A_z = -J_z \\ L_1: A_z = A_0 \\ L_2: \frac{1}{\mu}\frac{\partial A_z}{\partial n} = h \end{cases}$$

The model is composed of the control equation and boundary conditions. L1 applies the Dirichlet boundary condition. L2 applies Neumann boundary conditions. Then the functional equation about Az is:

$$\begin{cases} I_1(A_z) = \int_\Omega [\frac{1}{2\mu}(\nabla A_z)^2 - J_z A_z] d\Omega - \int_{L_2} A_z h ds \\ A_z|_{L_1} = A_0 \end{cases}$$

Functional equations do not contain constraints on the first Dirichlet boundary conditions. The approximate function of element free Galerkin method belongs to the fitting function. The Dirichlet boundary condition is equivalent to given the value of the function. The approximate value approach to original function value instead of completely coincident. Therefore, we should use Lagrange multiplier method or Penalty method for the boundary conditions. For L1, the penalty function is:

$$I_{L_1}(A_z) = \frac{1}{2} c_0 \int_{L_1} (A_z - A_0)^2 ds$$

The factor of Penalty function C is a relative large value, when minimize , the value of the points on the boundary will limit to the set value and realize the purpose of imposing boundary conditions.

Functional equations for the entire field:

$$I = I_1(A_z) + I_{L_1}(A_z)$$

Therefore, Az can be expressed as an approximate function:

$$A_z = \sum_J^n \Phi_J A_{zJ}$$

Φ is the shape function. We can get:

$$\delta I_{L_1}(A_z) = c_0 \int_{L_1} (\delta A_z)(A_z - A_0) ds$$

Therefore, we can represent all the equation by a matrix and a vector:

$$KA_z = F$$

With:

$$K_{I,J} = \int_\Omega \frac{1}{\mu}\left[\left(\Phi_I\right)_x\left(\Phi_J\right)_x + \left(\Phi_I\right)_y\left(\Phi_J\right)_y\right]d\Omega + c_0\int_{L_1}\Phi_I\Phi_J ds$$

$$F_I = \int_\Omega J_z\Phi_I d\Omega + \int_{L_2}\Phi_I h ds - c_0\int_{L_1}\left(\Phi_I A_0\right)ds$$

3.6. Results: 2D simulation

The procedures have been shown in the follow flow chart:

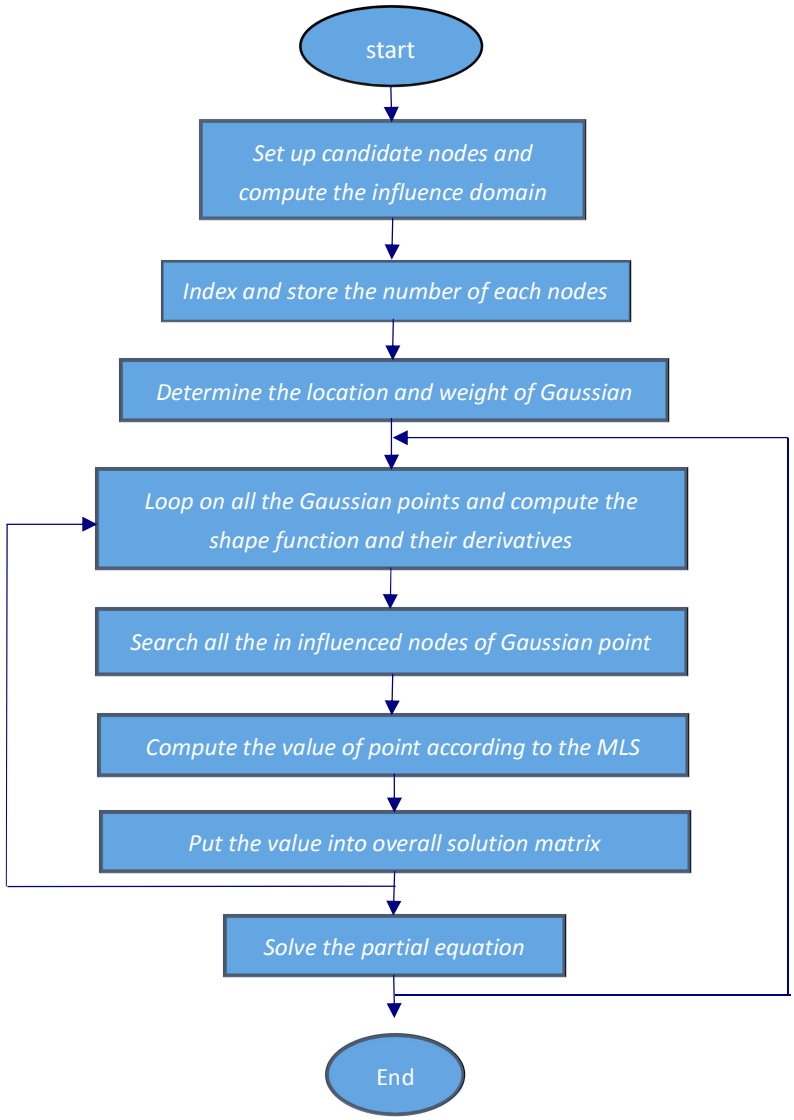

Table 3.1 flow chart of the simulation

As Fig. 3.3 shown below, a 2-dimensional has been designed as a square plate with a small square hole and a circle hole. The size of the plate is 400 x 400. The radius of the small circle is 60 and the center of the circle locate at (-80, 80). The size of small square is 120 x 120 and the center locate at (100, -100).

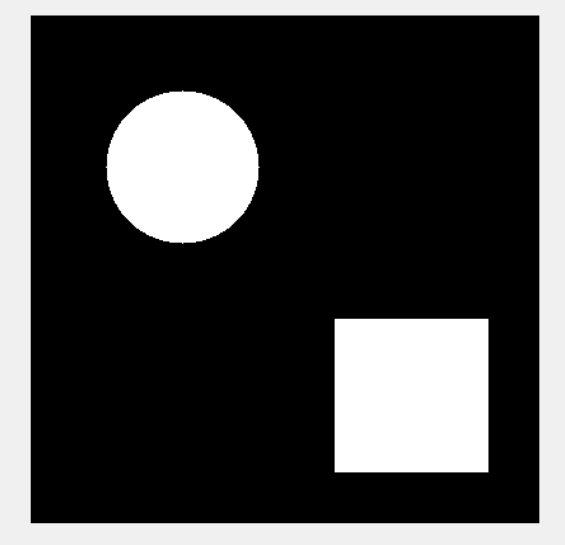

(a). 2-dimensional model for impingement damage

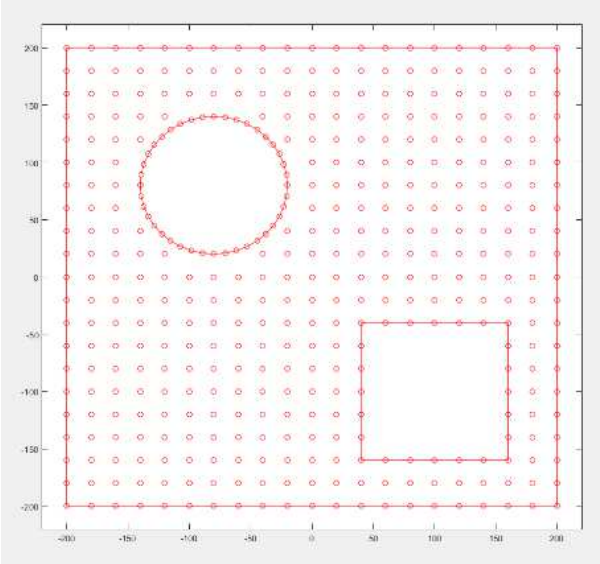

(b). EFG nodes set up

Figure 3.3 Simulation geometry for piping impingement damage using simplified 2D model

First, 21 x 21 nodes are arranged in the domain. The nodes locate in the hole will be ignored and serval nodes are arranged on the bounty of the circle. The approximation value of any points in this domain is fitting by these nodes. Then domain is divided into several sub domains, which is independent with the arrangement of nodes, but only for the completion of the regional integration. For each sub domain, repeating the follow steps: Find a Gaussian points within the sub domain and calculate its shape function which is influenced by the nodes within the influence domain. Calculate the vector F and the matrix k. The matrix K and vector F of the Gauss point are stored according to the point location Integrated into the overall solution matrix. When all the Gaussian points within this sub domain have been calculated, we move to next sub domain until the calculation in all the sub domains have been done.

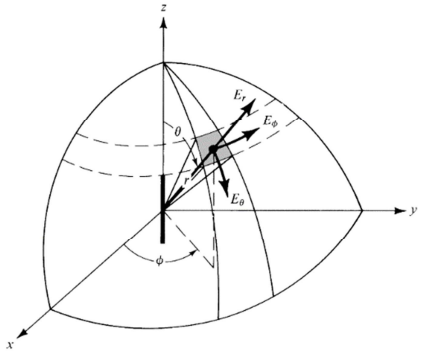

Figure 3.4 Illustration of electrical field orientation

Equations used for near field calculation is shown below.

$$\left.\begin{aligned} E_r &\cong -j\eta \frac{I_0 l e^{-jkr}}{2\pi k r^3}\cos\theta \\ E_\theta &\cong -j\eta \frac{I_0 l e^{-jkr}}{4\pi k r^3}\sin\theta \\ E_\phi &= H_r = H_\theta = 0 \\ H_\phi &\cong \frac{I_0 l e^{-jkr}}{4\pi r^2}\sin\theta \end{aligned}\right\} \quad kr << 1$$

I_0 is the current, ηis the intrinsic impedance. Simulation result shows good agreement with experiment measurement.

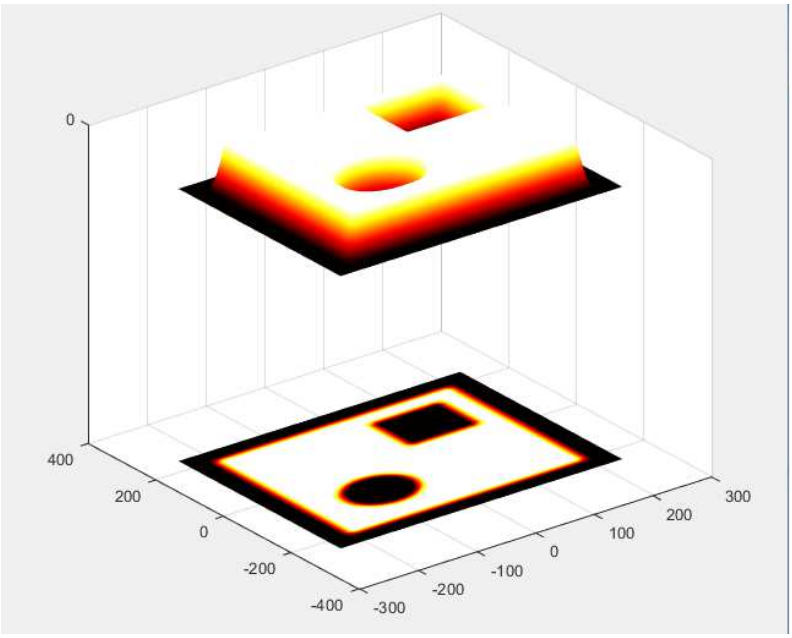

Figure 3.5 Simulation result

CHAPTER 4 Imaging optimization and comparison with DIC results

4.1. Experimental measurements and sensing development

Measuring the amplitude, or the intensity, of the reflected signal is one of the important parameters which one can measure. The localized reflected microwave amplitude carries information about the complex dielectric constant of the material. Using a sharp antenna tip results to acquiring data with high special resolution. In our experiment the probe, in many cases a coaxial tip antenna CTA, is brought within close proximity of the sample surface, and the sample is illuminated with microwaves at 7 GHz. The microwaves experience changes relative to the incident waves. Changes are tightly related to the dielectric properties of the PA and PE sample. It should be noted that the resolution is directly related to the tip geometry. Using sharper tips result to confining sample interaction area which lead to a better resolution. We used the raster scan technique to scan the sample and reconstruct the 2D images which are shown in the result part. The experiment set up is shown in Fig. 4.1.

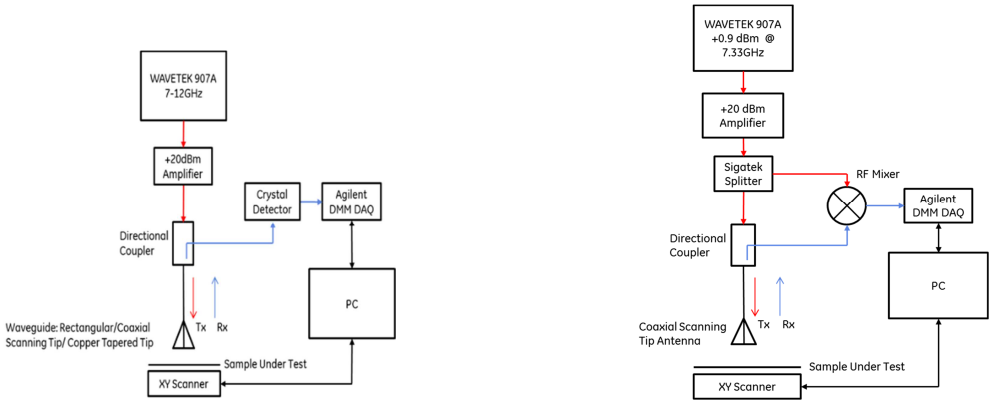

Amplitude Detection Setup Phase Detection Setup

Figure 4.1 Amplitude and Phase Detection Setups

The images obtained from PA and PE samples successfully demonstrated the use of microwaves in the near-field range for damage detection for piping materials. The resolution of these images depends on the shape and size of probe tip and the distance between probe tip and target. Current Research is focused on using Co-axial cable antenna which has been initially demonstrated that it can obtain better scanning results comparing to other probe types like open

ended waveguide. But the inner conductor of the co-axial cable is not mechanically solid enough to perform any contact scan, which we believe can improve the resolutions further and acquire surface topology as well. The PA and PE samples were scanned at 7GHz as the defects were hidden beneath the sample as shown in the following figures.

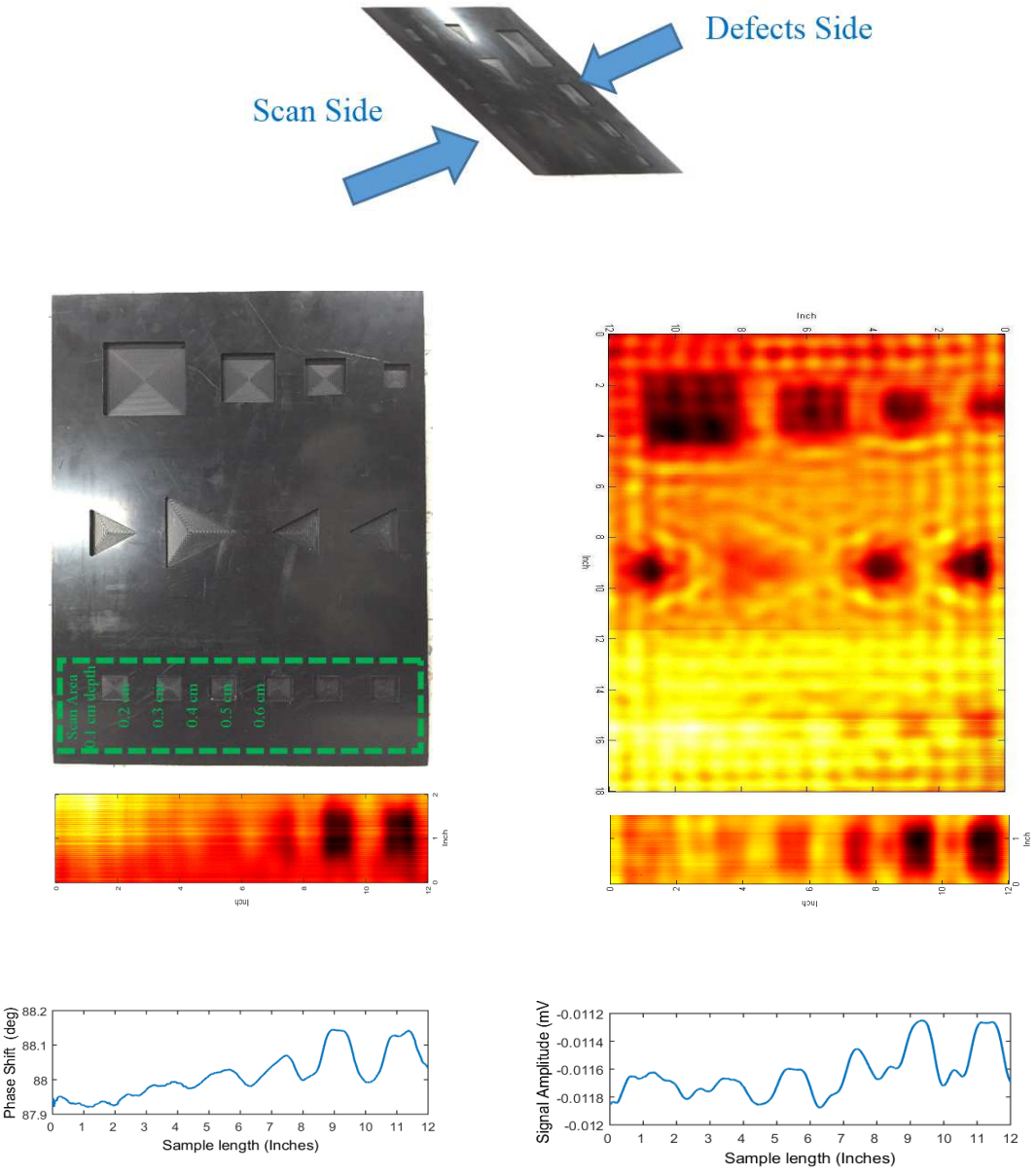

Phase measurement Amplitude measurement

Figure 4.2 Polyamide (PA) sample reconstructed images

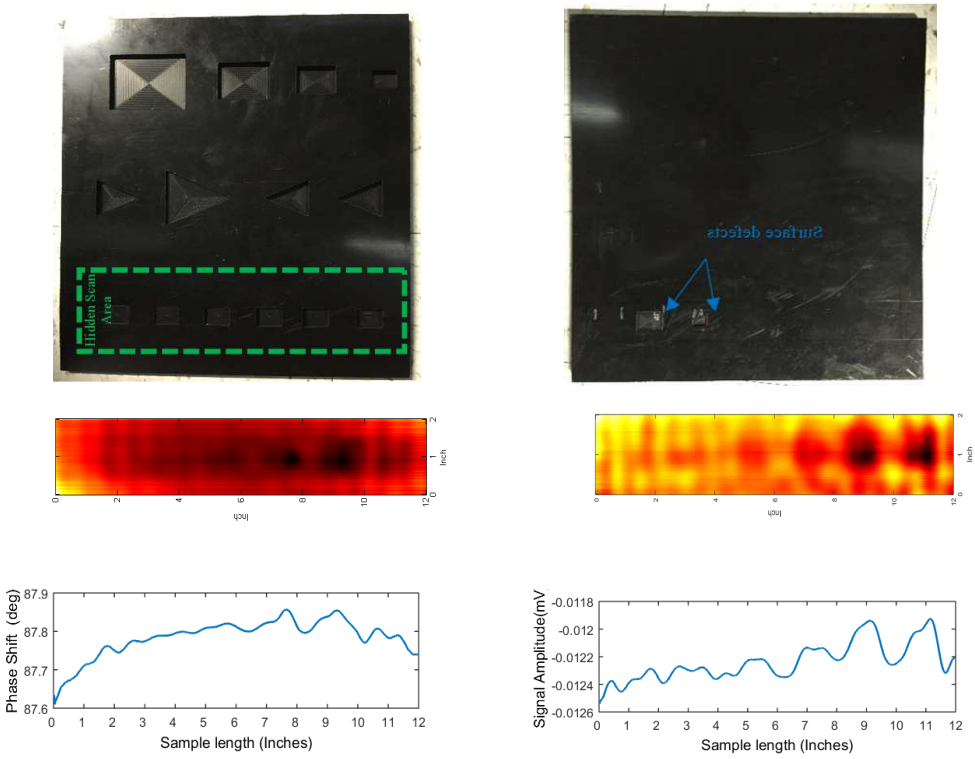

Phase measurement Amplitude measurement

Figure 4.3 Polythene (PE) sample reconstructed images.

Near field microwave imaging is far better resolution than the far filed. Amplitude and phase information were retrieved with high special resolution. Phase information extraction using frequency mixing is inexpensive, easy to implement approach. Using RF Siga Tek SM1717. This approach was capable to extract phase information of the scanned sample to construct 2D images that represent variation in the sample properties. Primary high resolution Images were abstained and presented in this report. Different damage signal signatures were observed for PA and PE samples. Raw data will be provided to ASU team for further probabilistic analysis. Currently, LEAP team is also pursuing to improve scan efficiency. The team is working to utilize fast imaging capability using sparse signal reconstruction, e.g. compressed sensing based approach to improve scan timing as well as image resolution. A multichannel model is been developed where the antenna array is configured with different geometries. A 3D simulation study for the cylindrical array was simultaneously conducted using FEKO software.

4.2. comparison with DIC results

In Q5, we performed near field microwave scan of both full specimens (without any hole) and notched specimens (specimen with hole) from industry collaborators. The resulting image of four notched specimens is shown below in Fig. 4.4.

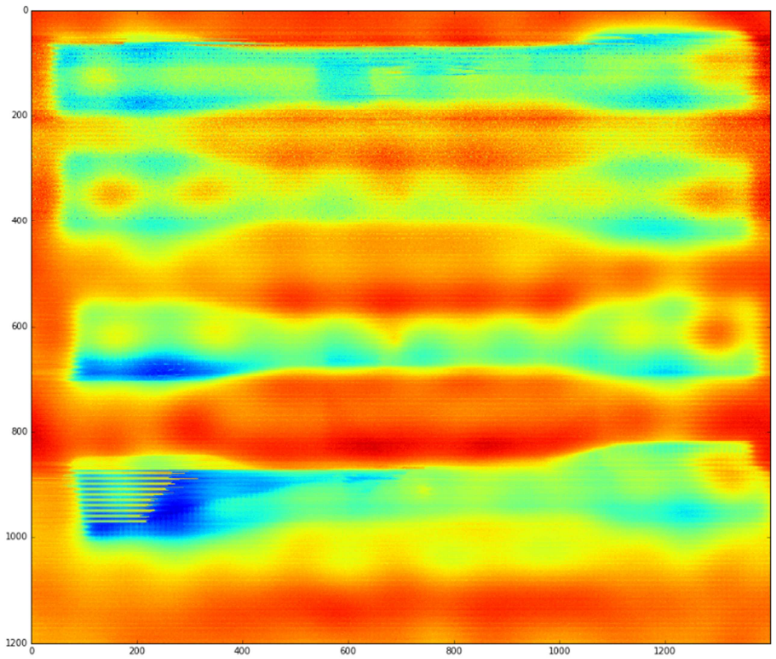

Figure 4.4 Near-field microwave scan of notched specimens

As the image shown above, the four specimens from top to the bottom are 70%, 50%, 30%, 0% of maximum value of displacement at fracture to which the specimens are elongated, respectively.

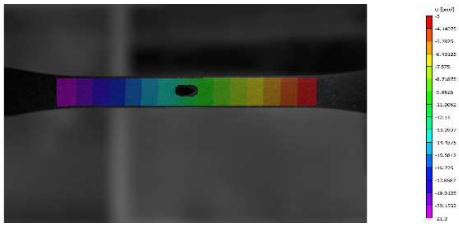

(a).U (mm) displacement

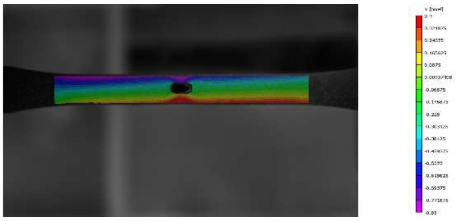

(b).V (mm) displacement

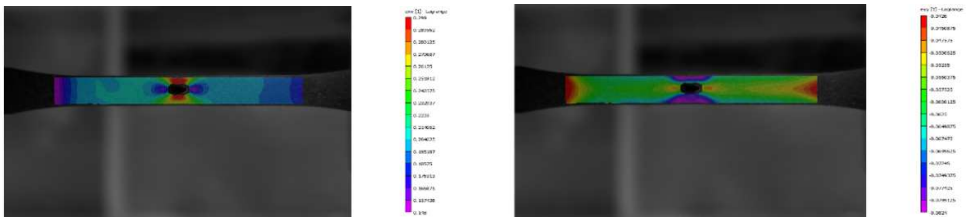

(c).local strain - X (exx) (d). local strain - Y (eyy)

Figure 4.5 tensile images of 0.7 notched specimens from Arizona State University

Fig. 4.5 shows the tensile test data notched specimens elongated at 70% of maximum value of displacement at fracture. A preliminary comparison has been shown in Fig. 7. As we can see in the image, both of the two image display a changing value around the hole. Also, they are both centrosymmetric.

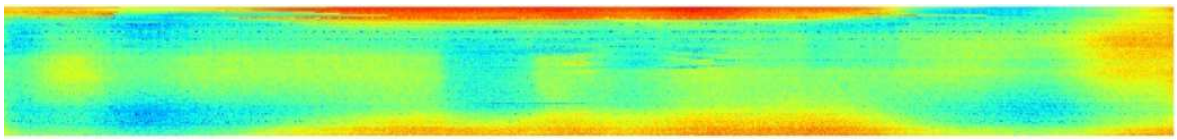

(a)

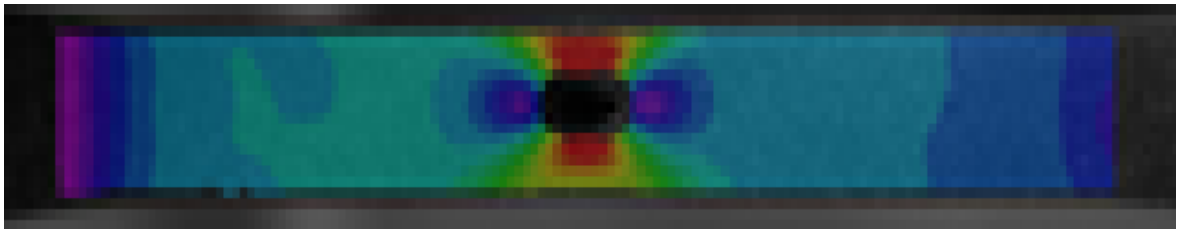

(b)

Figure 4.6 Preliminary comparison of NS 0.7

:(a) NFMM results and (b) DIC results

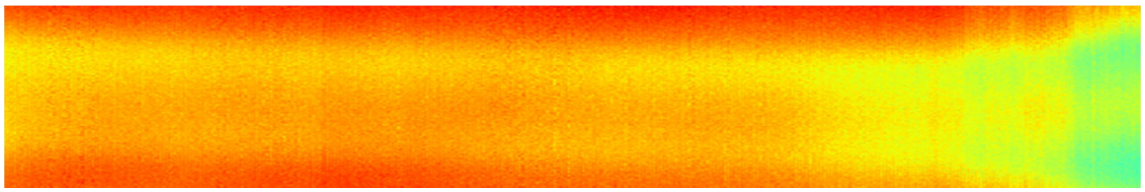

(a)

(b)

Figure 4.7 Preliminary comparison of FS 0.5

: (a) NFMM results and (b) DIC results

For full specimen (without any hole) shown in figure 4.7, we can see that none of them are centrosymmetric. The values in two images are both changing smoothly.

CHAPTER 5 EXPERIMENTAL TESTING

This work examines the failures of plastic pipelines due to surface damage by employing an integrated experimental and numerical simulations approach to asses effects of surface damage by notch sensitivity studies. The surface damage may be introduced due to rock impingement, excavations. The notch sensitiveness on the mechanical properties of Polyamide 11 (PA11) and Polyethylene (PE), which are popular pipeline materials, along with the comparative study on PA11 & PE materials are reported. A series of tensile testing were done in accordance with ASTM D638 standard on both PA11 & PE material specimens. To study the effects of surface damage on the mechanical properties of PA11 & PE materials, holes were drilled out at the centres of the specimens. The size and the depth of the holes (notches) of the samples were varied from medium level to severe level, with small, shallow holes & large, deep holes indicating medium & severe levels of notch respectively. From the tensile testing, values of Young's modulus, yield strength, peak stress, critical strain along with load displacement curves for PA & PE specimens were obtained. An extended finite element method (XFEM) with cohesive zone method (CZM) was employed to build the numerical model in ABAQUS/CAE to simulate the tensile testing of PA11 & PE specimens along with fracture which would enable better prediction of the impingement effects on the pressurized gas pipelines. The material model for the XFEM+CZM analysis was calibrated by utilizing the mechanical property data obtained from the ASTM D638 tensile test of PA 11 & PE specimens (specimen without any holes). Similar to the experimental work carried out, XFEM+CZM analysis was executed on the PA11 & PE impinged specimens, to validate the results from the numerical model by comparing with the results from the experimental investigation. Digital Image Correlation (DIC) technique was used to obtain the contour strain & displacement plots during the tensile testing of the specimens. The results from the DIC analysis were compared with that from the numerical simulations.

A drastic reduction in the critical strain value was observed of both PA11 & PE notch samples were observed. This may be attributed towards formation of stress concentration region around the impingement leading to premature failure of the specimen. Similar trends were observed for the peak loads of the impinged samples. However, the PA11 specimens with medium level impingement were observed to show higher resistance to failure than the PE specimens subjected

to similar testing conditions indicating that the PA11 material is a better candidate for pipelines to resist failures due to rock impingements. The XFEM+CZM numerical model was calibrated and good agreement was found between the experimental & numerical results thus indicating the validity of the numerical model. The comparison of the DIC strain values and strain values from numerical model also showed a good agreement. This numerical model when implemented on pressurized pipeline model would better predict the impingement effects on the pipeline.

5.1. Background of Tensile Testing of Plastics

The testing of plastics includes wide variety of thermal, chemical and mechanical tests. This particular article reviews the standardized tensile testing method i.e. ASTM D638 along with the various practices adopted by engineers and scientists to test for the tensile properties of plastics. Tensile test embraces various procedures by which modulus, strength and ductility can be assessed. Generally, the term 'tensile test" means a test wherein a slender specimen is extended uniaxial at a uniform rate. Ideally, specimen should be slender with constant cross section across the gage length, free to contract laterally and expand longitudinally. Though this test was initially designed for testing metals, it was later adopted and adapted for testing plastics and polymers. In the case of plastics, the adaptation had to encompass for the visco-elastic behavior, probable anisotropy of the product. The deformation mechanism of polymers differs from that of metals. In most polymers, only about half of the work of plastic deformation is liberated as heat.

In case of metals, the plastic deformation results in relative change of orientations and positions of metal molecules. So, the large amount of stored integral energy of the polymers have many effects not seen in case of metals. One consequence is, when an unconstrained polymer that has undergone plastic deformation is heated, it will contract toward its original length. The ultimate tensile strength of most of the plastics ranges from 50-80Mpa. The mechanical behavior of polymers is a function of temperature as well as time. So, the data based on short term test have possibility of misinterpreting the results of tested polymers in a design application involving long-term loading conditions.

Plastics are visco-elastic materials, in which deformation can be dependent on temperature as well as time. Probable anisotropy in the plastic can affect the tests [2].

Viscoelasticity: The time dependence of the deformation of visco-elastic materials can be

attributed to rate at which stress is applied. The temperature dependence will depend on the properties of plastic itself which are different for amorphous, crystalline and semi-crystalline [3] [4]. As a result, during the tensile test the specimen may distort near grips and clamping forces may relax with passage of time. The subsequent force displacement curves obtained from the tests performed would have time dependence as well as effect of strain rate incorporated. To this effect, Reis et al proposed a model and validated them to evaluate mechanical tensile properties at different strain rates for HDPE [5]. Serban et al reported that for semi crystalline polymers temperature & strain rate changes affects Young's modulus the most with minimal impact on tensile strength [6].

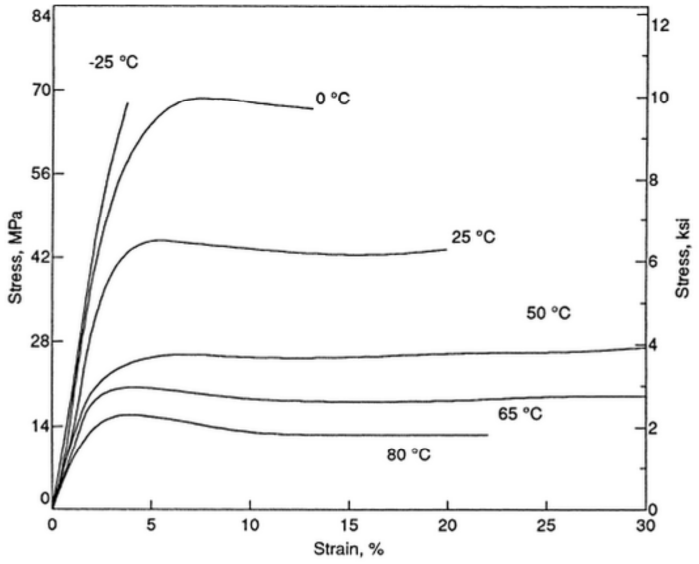

Figure 5.1: Influence of Temperature on Stress- Strain curves, Stain rates have a similar effect [2]

Anisotropy: Due to anisotropic behavior of certain plastics, the specimens under investigation have a tendency to deform in irregular ways and may break at points other than those which have minimum cross-section. There are chances that failure takes place at the grips unless special precautions are taken. So, as a result of which the moduli and strength may be higher or lower than expected due to this anisotropy that may be introduced by flow geometry [7]. Recent work on this by Dyamenahalli et al in the characterization of shape memory polymers for tensile properties conclude that for anisotropic polymers which have discontinuous phase requires use of biaxial testing systems [8].

5.2. Uniaxial tensile test ASTM D638

ASTM D638 is one of the more popular mechanical tests of plastics employed to determine tensile properties of unreinforced and reinforced plastics [9] under specified shape, condition of pre-treatment, temperature, humidity and testing machine speed. This test is designed to produce tensile property data for control & specifications of plastic materials. Important parameters from this test include ultimate tensile test (UTS), Young's stress, Poisson's Ratio, elongation at yield [8]. Data from this test has been found useful in engineering design with a precaution that data cannot be exactly used for design calculations if the environment of use is different from that of testing.

Recent works on polymer tensile testing conducted in controlled environment include:

- El Mourid et al – performed D638 tensile tests on aged polymer matrix composites at maximum service temperature to evaluate degradation of polymer matrix and performed tests in two different directions to explore anisotropy of the material [10].
- Sadeghian et al – performed D638 tensile testing on welded Acrylonitrile butadiene styrene (ABS) sheets. In order to avoid defects in the weld joint, samples were prepared from core of weld joints [11].

Specimen Preparation: One of the important parts of D638 is specimen preparation. Care should be taken to ensure all samples are prepared in exactly the same way. Because mechanical properties are sensitive to temperature and absorbed moisture, conditioning procedure for test specimen have been developed and defined in ASTM D618 & ISO 291. ASTM D638 has laid down specimen drawings with five types of dimensions depending on the desired thickness and testing conditions.

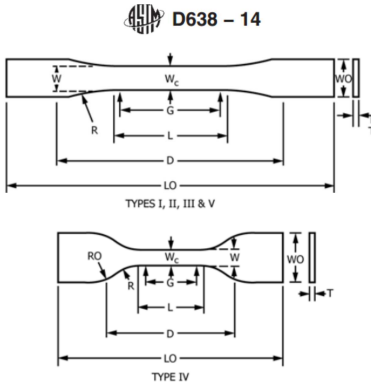

Dimensions (see drawings)	Type I
W—Width of narrow section[E,F]	13 (0.50)
L—Length of narrow section	57 (2.25)
WO—Width overall, min[G]	19 (0.75)
WO—Width overall, min[G]	...
LO—Length overall, min[H]	165 (6.5)
G—Gage length[I]	50 (2.00)
G—Gage length[I]	...
D—Distance between grips	115 (4.5)
R—Radius of fillet	76 (3.00)
RO—Outer radius (Type IV)	...

Figure 5.2: Dimension and shape Type 1 specimen from ASTM [20]

5.3. Experimental Testing Procedure

In total, tensile tests were performed on 30 samples of PA-11 & PE using a universal testing machine (make: MTS Alliance 10/R) as presented in fig. 3. The ultimate tensile strength, % elongation, yield strength (at 0.2% strain), and Young's modulus of each of the specimens at 0.2 in/min strain rate and 3.75" gauge length was measured for each specimen.

Strain measurements of each of the specimens tested were accomplished by optical technique, namely Digital Image Correlation (DIC). DIC is an optical method that employs tracking and image registration techniques for accurate 2D and 3D measurements of changes in images. This is often used to measure deformation, displacement, strain, and also optical flow, but it is widely applied in many areas of science and engineering. Images were captured using Lumenera Infinity 2 Camera. The captured images were analysed by commercial DIC tool called Vic-2D.

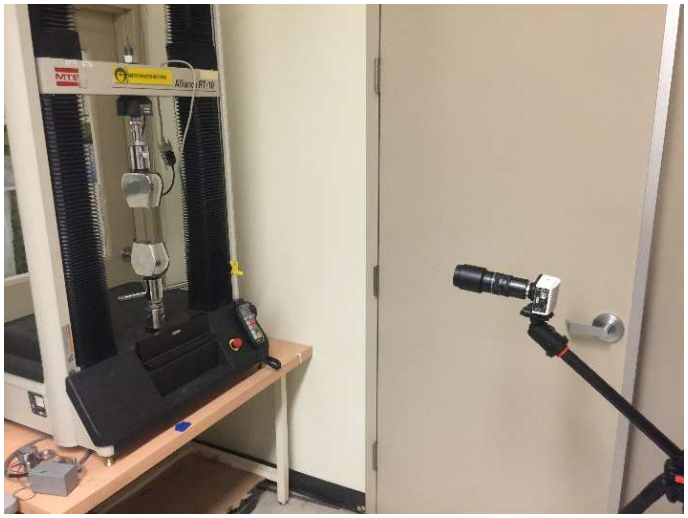

Figure 0.1 : MTS Universal Testing Machine along with camera & PA11 (black), PE (white) specimen (below)

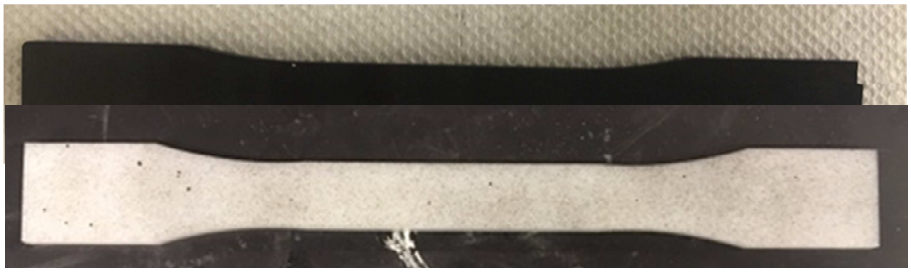

5.4. Test specimen preparation

Test specimens of ASTM Type 1 were used in the short term tensile testing. The material used for the testing were PA11 & PE. Two sets of specimens were prepared.

a) In order to introduce an impingement, holes were drilled at the mid-section of the specimen. The circular holes, which were of varying size and depth, were drilled by the NC Machining center as shown in fig. 4. The maximum and minimum diameter of the hole were ¼'' & 1/8'' respectively. With regards to depth of the hole, it was either a through hole or a hole that was as deep as half of the specimen's thickness. Speckle pattern were created on each of the specimens for DIC strain measurements.

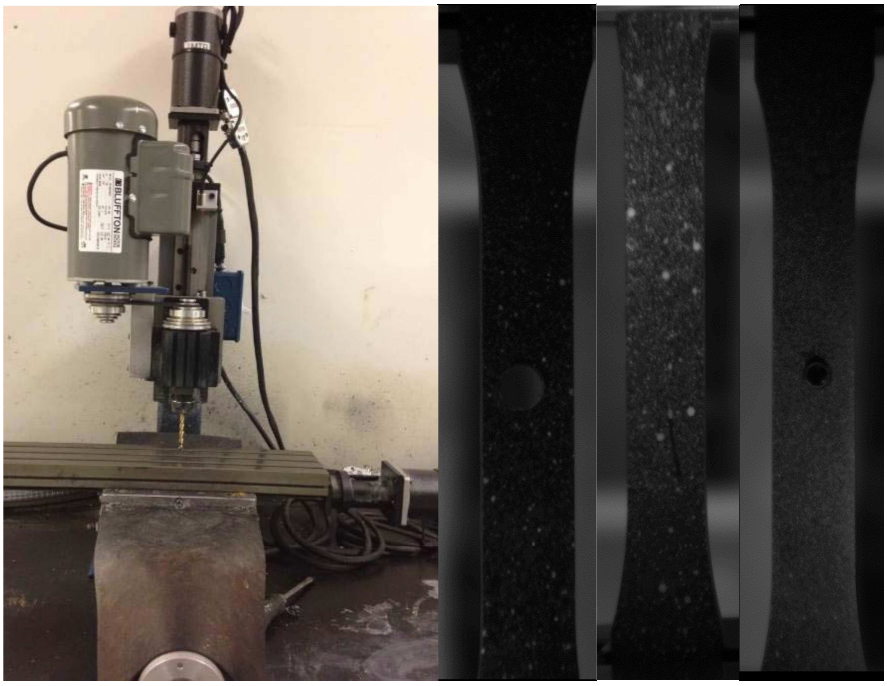

Figure 0.2: NC Drilling Machine and specimens with and without holes of varying size and depth.

Specimen No.	Depth of impingement [a]	Diameter of impingement
N1	0	0
N2	0.12''	¼''
N3	0.12"	1/8''
N4	0.06"	¼''
N5	0.06"	1/8"
N6	0.06"	1/8"
N7	0.06"	1/8"

Table 0.1: Tensile test matrix

b) Indented Specimens were prepared using the Automated Ball Indenter (ABI) fixed to the MTS universal testing machine. The extent of indentation is as shown in Table 2.

Fig. 5 shows the indented PA11 & PA samples.

Specimen No.	Depth of Indentation (in.)
N1	0.055 (1.4 mm)
N2	0.063 (1.6 mm)
N3	0.071 (1.8 mm)
N4	0.079 (2.0 mm)

Table 0.2: Test Matrix for Indentation test

Figure 0.3: Indented PA-11 (left) & PE (right) specimen

5.5. Test specimen for diagnosis at CU Denver

PA-11 & PE samples were prepared for Non- Destructive Evaluations (NDE) to be carried out at CU Denver. Both type of specimen i.e. impinged & indented specimens along with smooth specimens were shipped.

Smooth specimen, impinged specimen & indented specimen was elongated up to 30%, 50%, 70% of the maximum elongation, for which the data were obtained from the stress-strain curves of PA11 & PE smooth specimens.

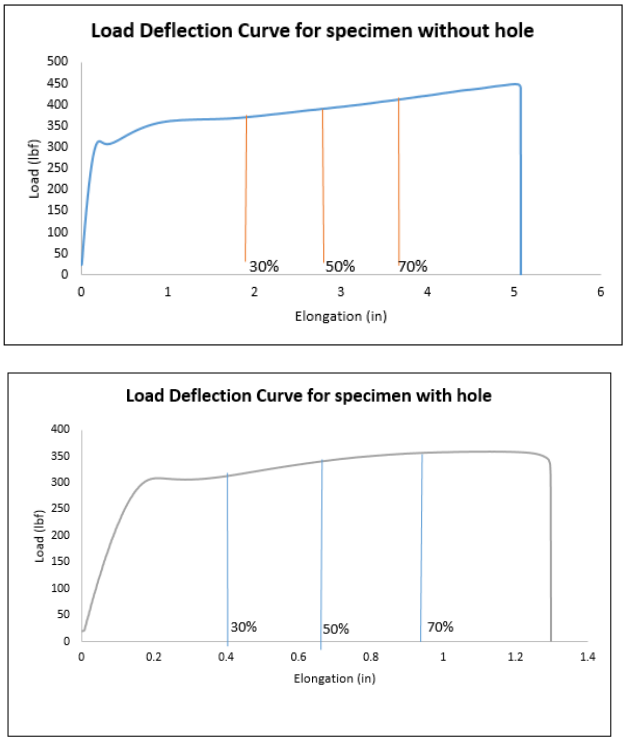

Figure 0.4: Load deflection curves indicating % loading for shipped specimen

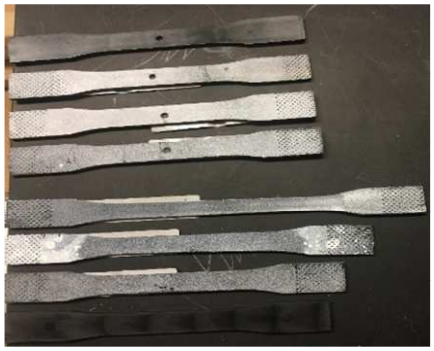

Figure 0.5: PA-11 Specimens smooth & notch for UC Denver

CHAPTER 6 NUMERICAL SIMULATIONS

The numerical simulations of the ASTM D638- Tensile testing were carried out in ABAQUS/CAE. Extended finite element analysis (XFEM) coupled with Cohesive Zone Model (CZM) was utilized to simulate the fracture of tensile specimens. In total, 15 simulations were carried out. Initially, the materials property data from the experiment was used to calibrate the material model for the smooth specimen by comparing with the experimental results. True stress-strain data was used for calibration. Then, using the calibrated model, simulations of the notched specimens was undertaken and was compared with the corresponding experimental results to validate the model.

Fig. 8 shows CAD model the central part of the dog bone specimen (gauge length) that was used for the analysis. Fig. 8 also shows the boundary conditions i.e. fixed boundary condition on bottom end and velocity (0.2”/min) boundary condition on the other end. The values of Young’s modulus, yield stress points post elastic region, max principal stress and displacement at failure (traction separations) data from the experiment were used to model the material. Two types of mesh elements, brick (C3D8R) and tetrahedral (C3D4) were used.

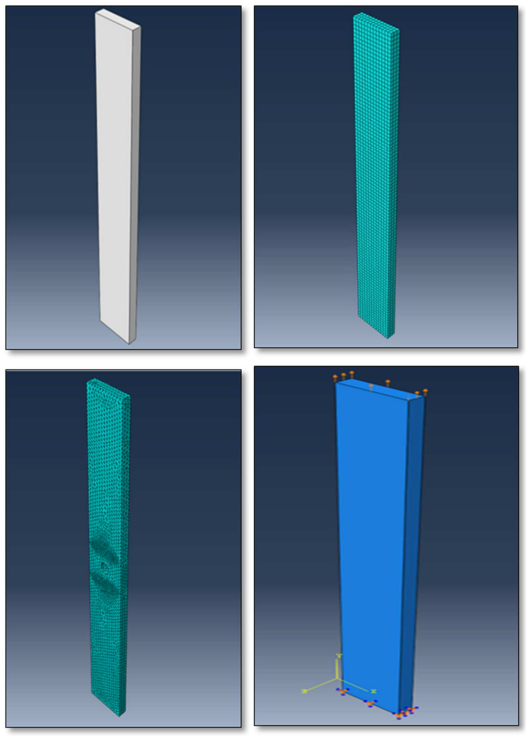

Figure 6.1: Simulations in ABAQUS showing the specimen model, meshing & Boundary Conditions

6.1. PA-11 Results

The results from the tensile testing is as shown in fig. 9. Table 3shows the values of peak loads and ductility for all the tested samples. It can be clearly observed that there is a drastic reduction in the critical strain values as the degree of damage increases, the fig. 10 further validates the point. Similar trend can be observed for peak load reduction with certain level of resistance in the medium level damage as seen in fig. 10. The average Young's modulus and Ultimate tensile stress for PA-11 was found to be about 1013MPa and 51MPa respectively.

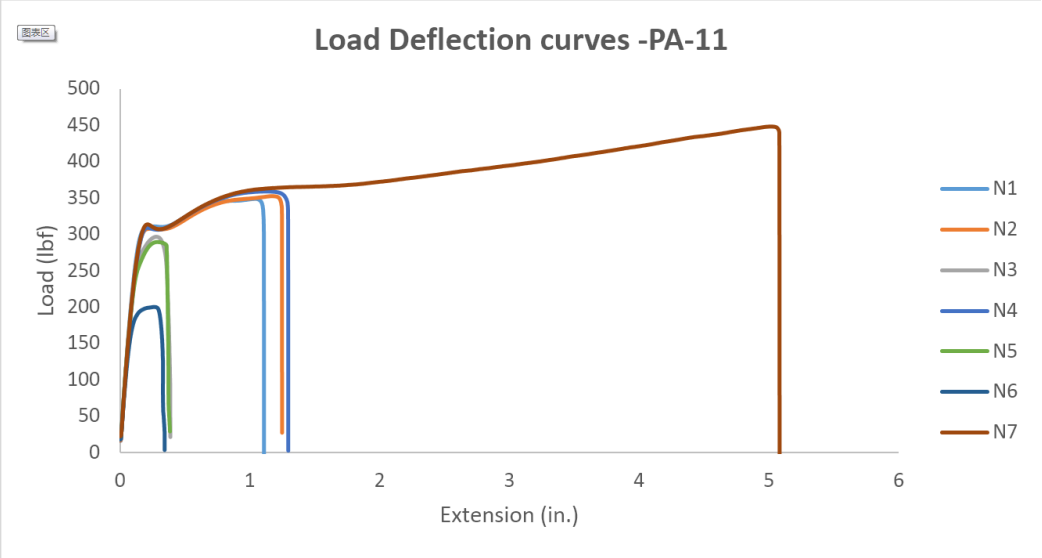

Figure 6.2 PA-11 Load deflection curves

Table 6.1 Results from ASTM D638 Tensile testing of PA 11

Specimen no.	Peak load(lbf)	Modulus(ksi)	% elongation
N7	448.27	147.79	135.54
N4	200.07	145.18	9.18
N3	296.75	158.96	10.34
N5	289.55	154.32	10.26
N1	348.90	153.30	29.61
N2	352.72	150.84	33.308
N6	359.01	147.36	34.59

Table 6.2 : Results from ASTM D638 Tensile testing of PA 11

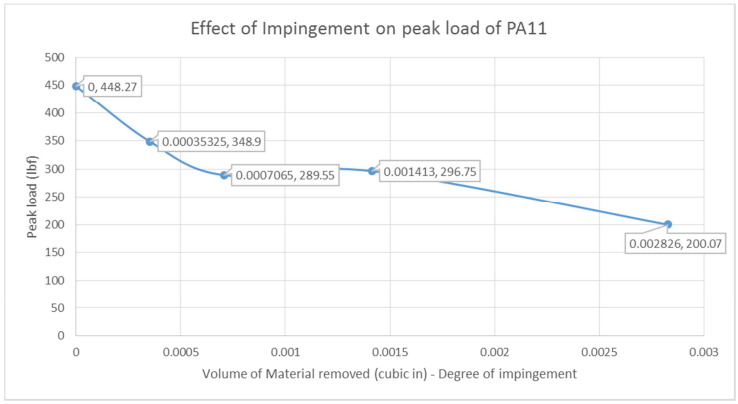

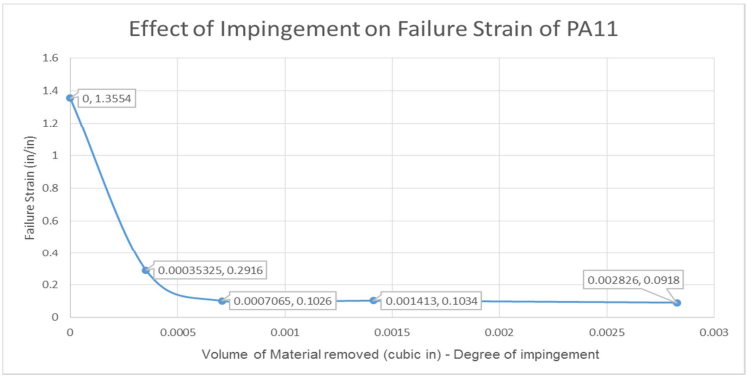

Figure 6.3: Effect of Impingement on PA-11 Specimen- Peak Load (top) & Failure strain (bottom)

Using the experimental data as shown in Table 8.3, material was modelled in ABAQUS for the XFEM+CZM simulations. Table 5 shows the results from experiment (DIC) and the numerical simulations.

Material Properties	**Values in SI units**
Young's Modulus	1013 MPa
Yield Stress	37.35 MPa
Max. Principal Strain	1.39
Max Displacement at failure	130 mm

Table 6.3: PA11 Material Properties

Testing & DIC	Numerical Simulations
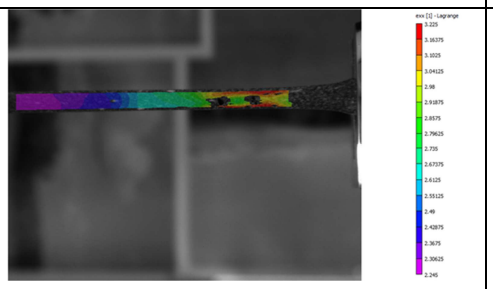	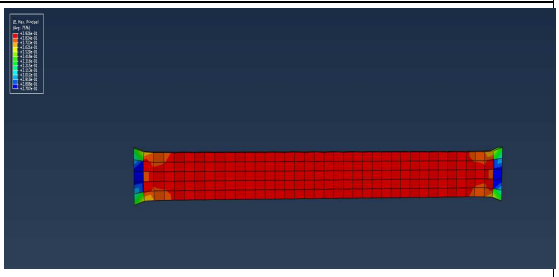
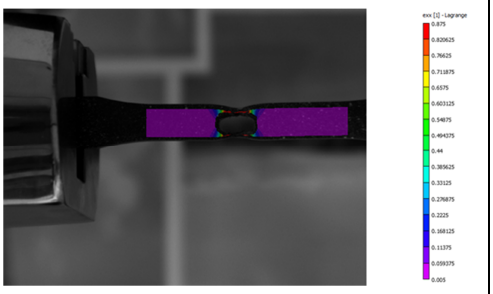	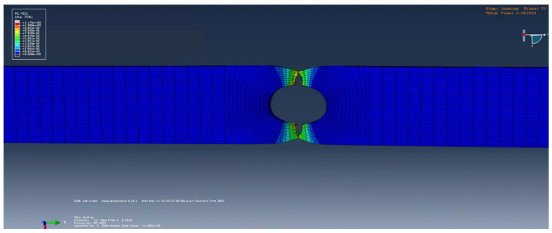
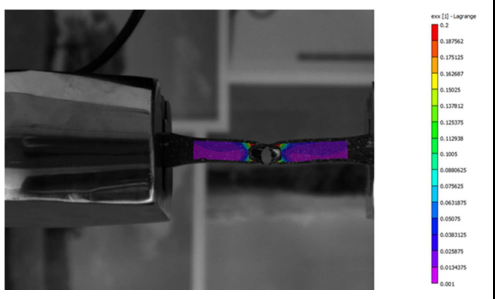	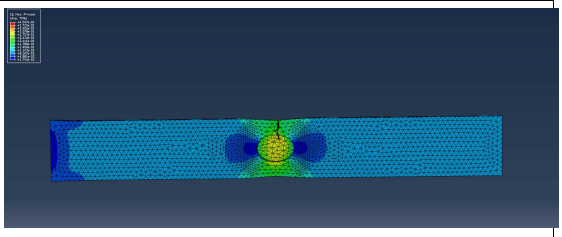
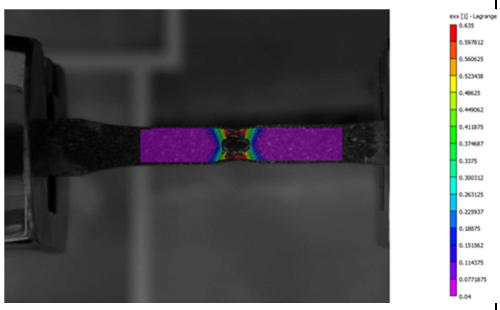	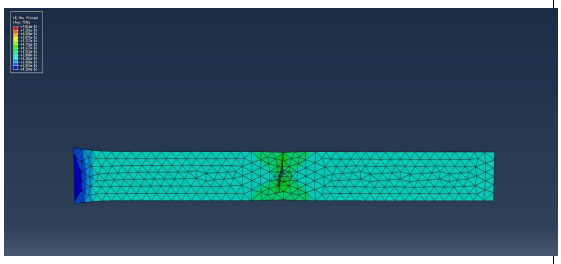
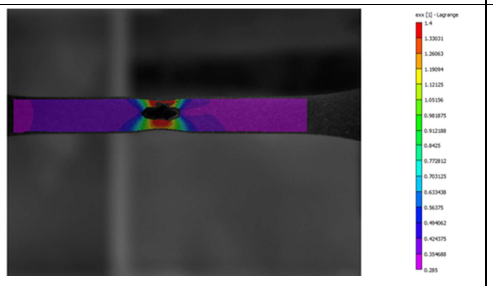	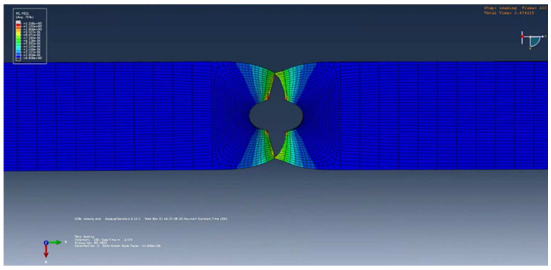

Table 6.4: Experimental (DIC) & numerical simulation results

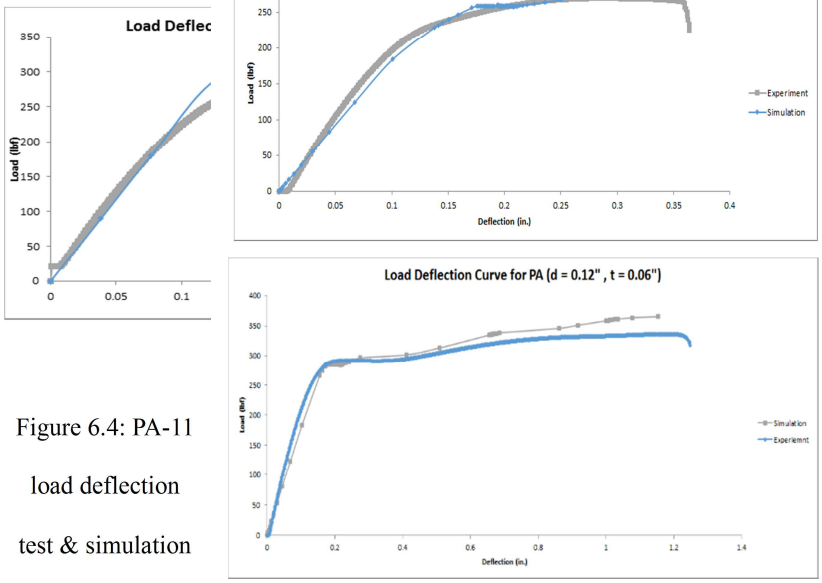

Figure 6.4: PA-11 calibration curve & load deflection curves comparing test & simulation results

Fig. 8.4 shows results comparing experimental and simulation cases. As seen, the calibration for the smooth specimen is accurate. There is a very good aggrement between the experimental & simulation results for the notch specimen cases, indicating validation of the model. The maximum error in results for peak load and failure displacement are about 8.5% and 8.4 % respectively.

The results from the indentation testing were found to be similar to the smooth specimen results indicating minimal effect of indentation on the material properties. One the reasons for this observation is the degree of recovery of deformation induced by the indentor resulting in very

minimal changes in the material properties when compared with the smooth specimen results.

6.2. PE Results

The results from the tensile testing is as shown in fig. 12. Table 6 shows the values of peak loads and ductility for all the tested samples. It can be clearly observed that there is a drastic reduction in the critical strain values as the degree of damage increases, the fig.13 further validates the point. Similar trend can be observed for peak load reduction with certain level of resistance in the medium level damage as seen in fig. 8.5. The average Young's modulus and Ultimate tensile stress for PE was found to be about 1140 MPa and 26 MPa respectively. The smooth PE specimen was not loaded till failure due to MTS machine limitations

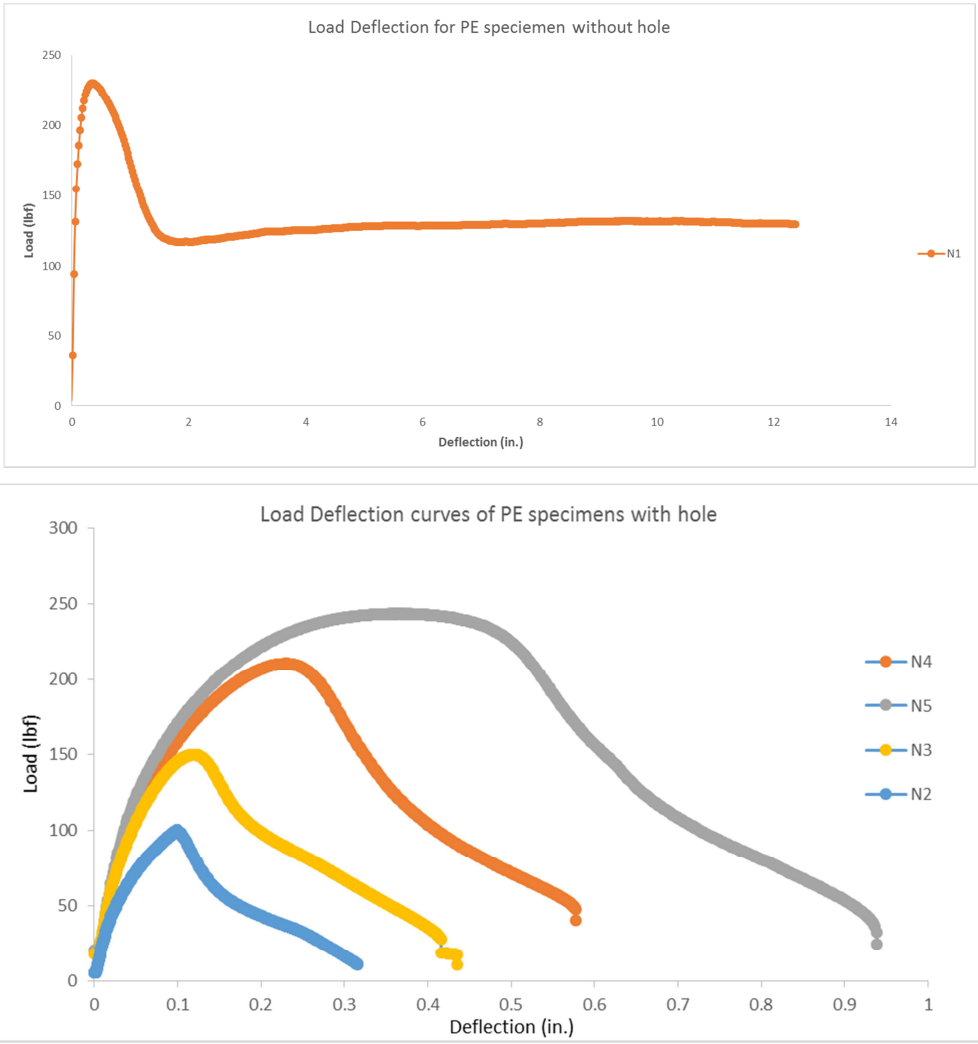

Figure 6.5: PE Load deflection curves

Specimen no.	Peak load(lbf)	% elongation
N1	245.32	n/a
N2	100.30	9.9
N3	150.12	11.18
N4	210.36	23.1
N5	243.34	36.7

Table 6.5: Results from ASTM D638 Tensile testing of PE

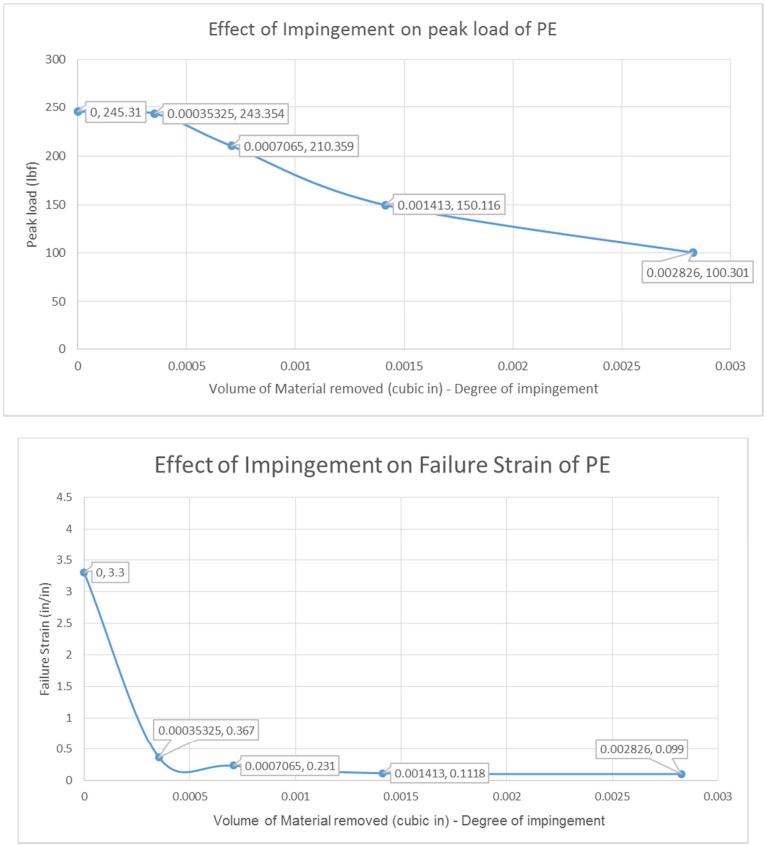

Figure 6.6: Effect of Impingement on PE Specimen- Peak Load (top) & Failure strain (bottom)

Using the experimental data as shown in Table 8.6, material was modelled in ABAQUS for the XFEM+CZM simulations. Table X shows the results from experiment (DIC) and the numerical simulations.

Material Properties	Values in SI units
Young's Modulus	1145 MPa

Yield Stress	27.56 MPa
Max. Principal Strain	2.2
Max Displacement at failure	200 mm

Table 6.6: PE Material properties

Testing & DIC	**Numerical Simulations**
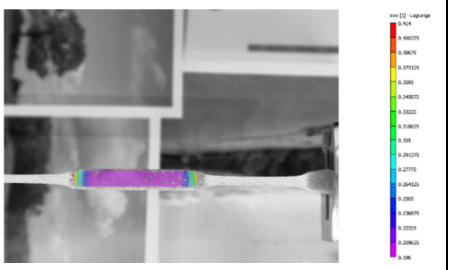	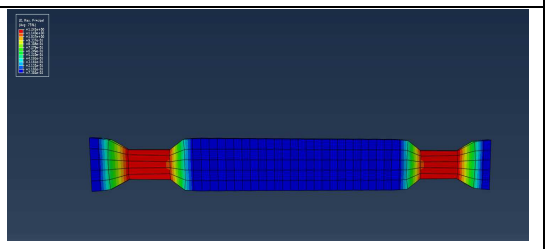
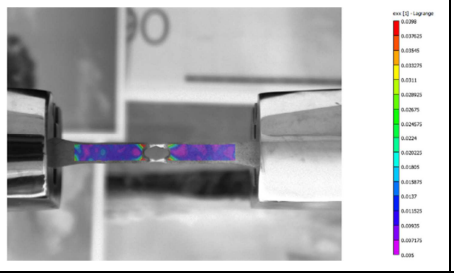	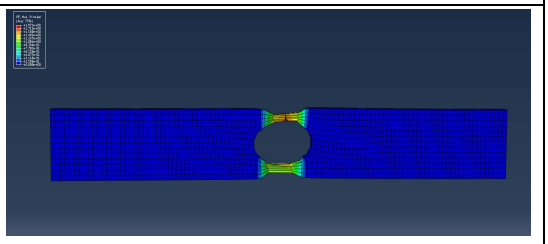

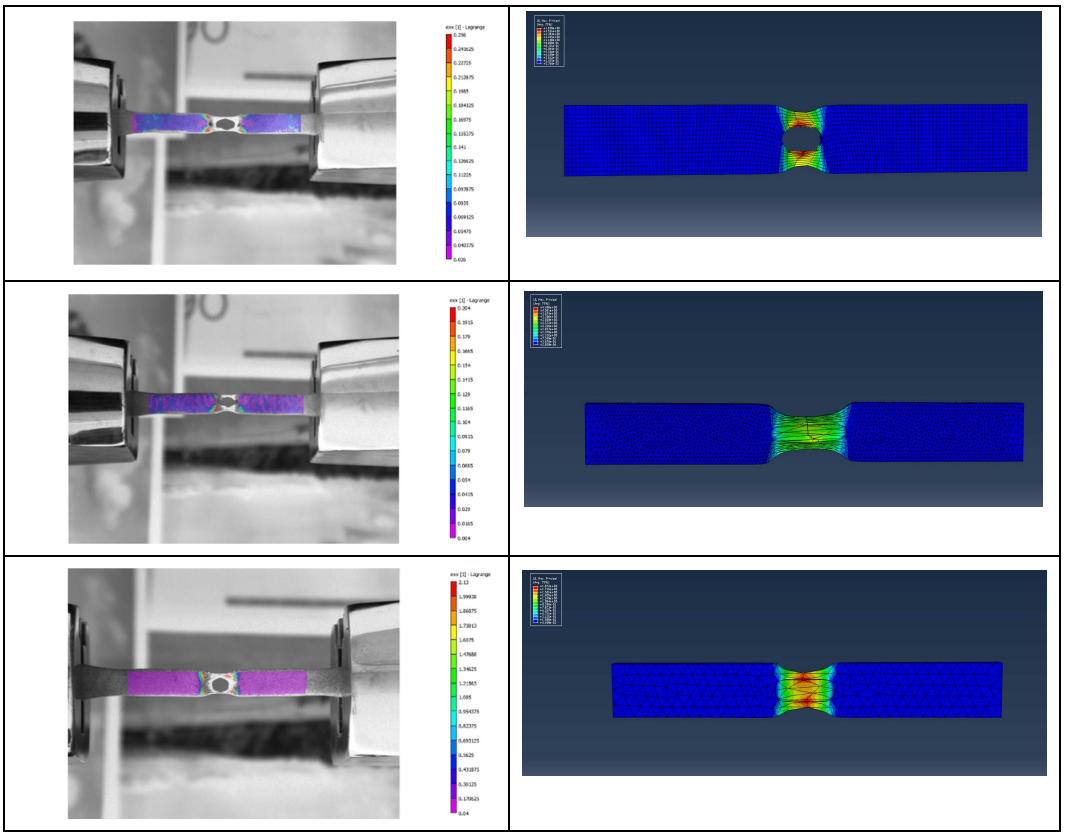

Table 6.7: Experimental (DIC) & numerical simulation results

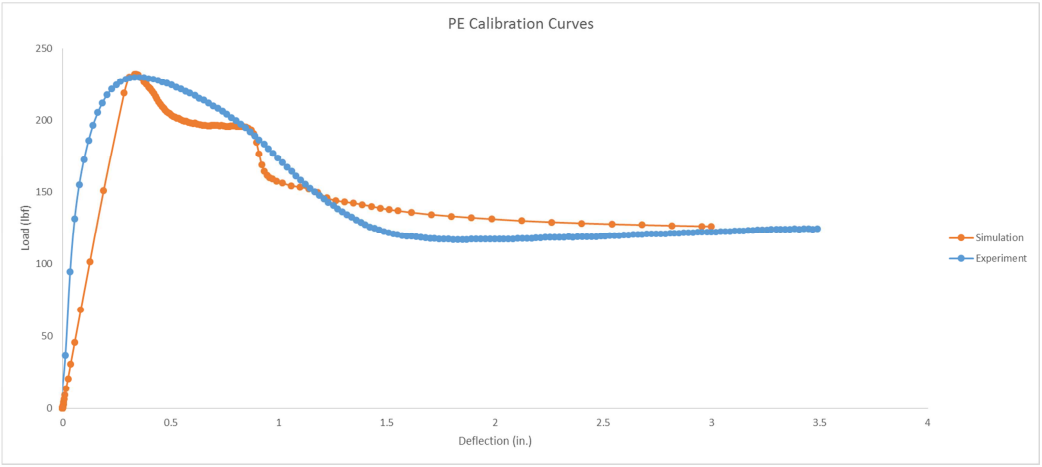

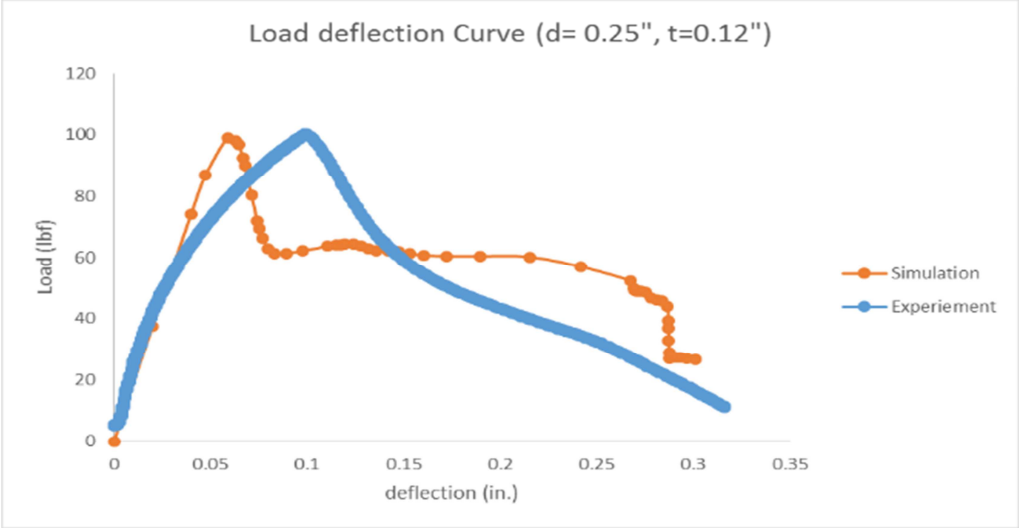
Load deflection Curve (d= 0.25", t=0.12")
Load (lbf)
120
100
80
60
40
20
0
0
0.05
0.1
0.15
0.2
0.25
0.3
0.35
deflection (in.)
Simulation
Experiement

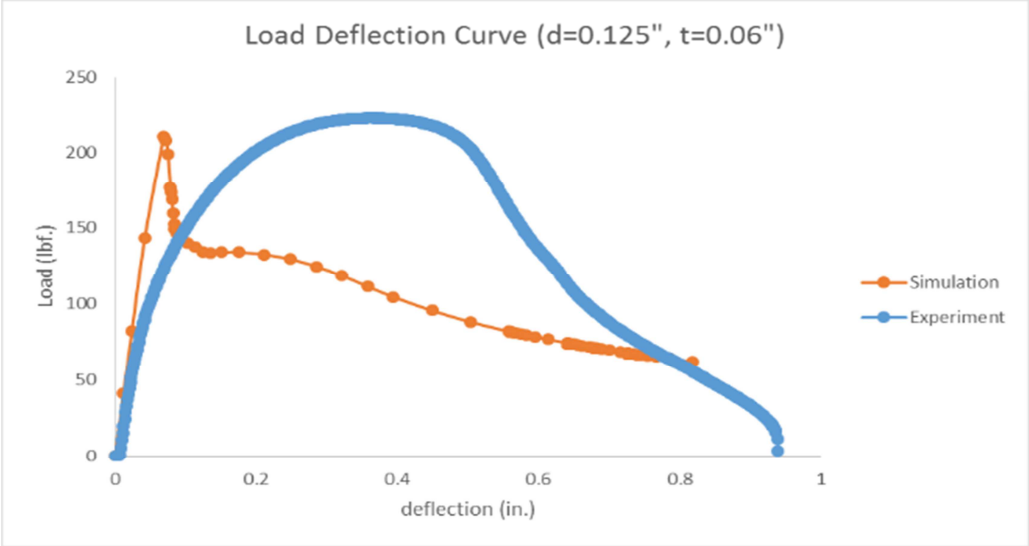
Load Deflection Curve (d=0.125", t=0.06")
Load (lbf.)
250
200
150
100
50
0
0
0.2
0.4
0.6
0.8
1
deflection (in.)
Simulation
Experiment

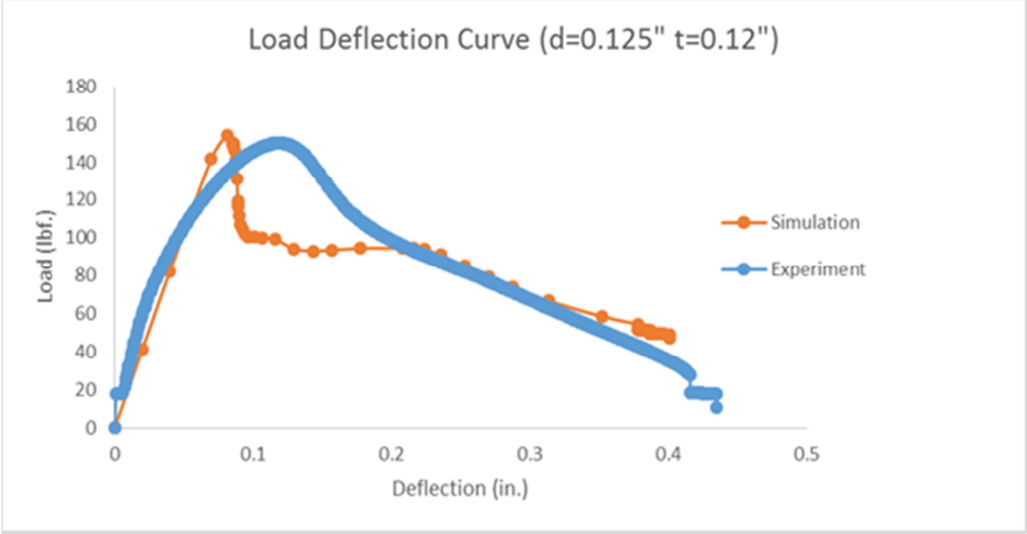
Load Deflection Curve (d=0.125" t=0.12")
Load (lbf.)
180
160
140
120
100
80
60
40
20
0
0
0.1
0.2
0.3
0.4
0.5
Deflection (in.)
Simulation
Experiment

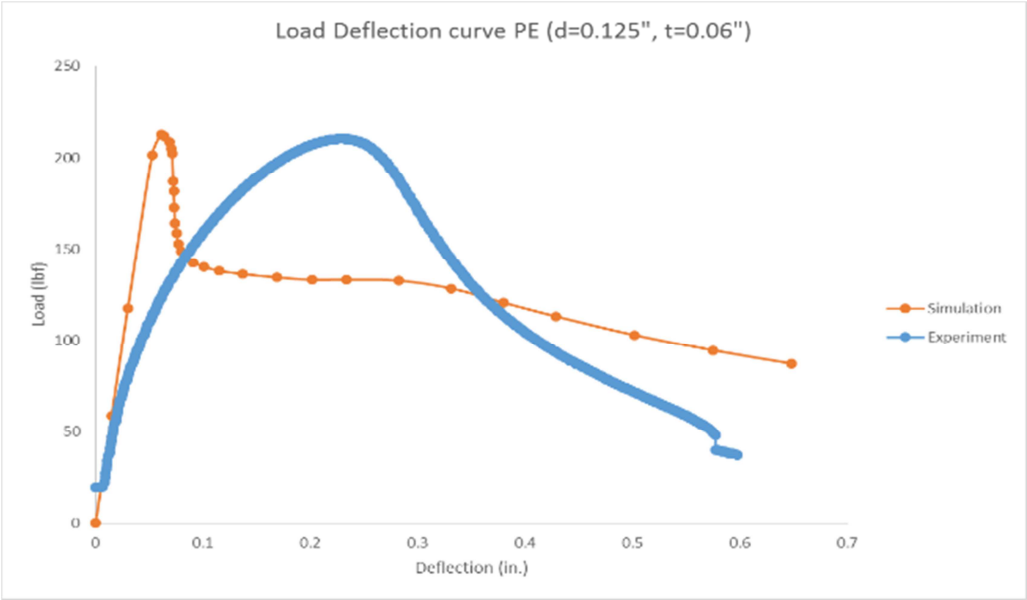

Figure 6.7: PE calibration curve & load deflection curves comparing test & simulation results (XFEM+CZM)

Fig. 8.7 shows results comparing experimental and simulation cases. As seen, the calibration for the smooth specimen is accurate. There is condiderble diffrence between the experimental & simulation results for the notch specimen cases, indicating need for advanced calibration models to be utilized.

POLYUMOD software was used to calibrate the PE true stress-strain curves. Using one of the material model available in the library, the PE curves were calibrated as shown in the fig. 8.8 This material was imported into ABAQUS as a user material (UMAT) to carryout the simulations. However, to undertake XFEM+CZM simulation the calibrated material model from POLYUMOD should be integrated with the traction seperation properties and a fused user material (UMAT) script is to be used. But, only classical finite element analysis (FEA) was carried out to verify the experimenal results without fracture. As seen , fig.8.8 shows calibration to certain extent with experiemntal data. A good aggrement was found between the experimental and the FEA simulated reults for notched specimen as seen from fig. 8.9.

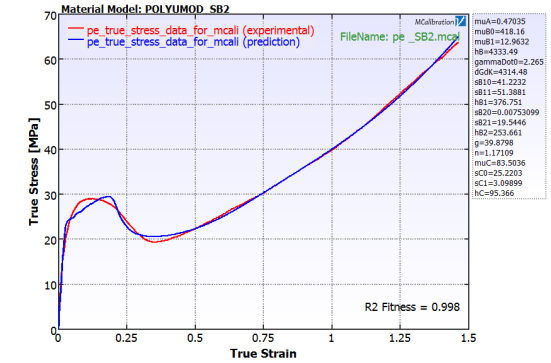

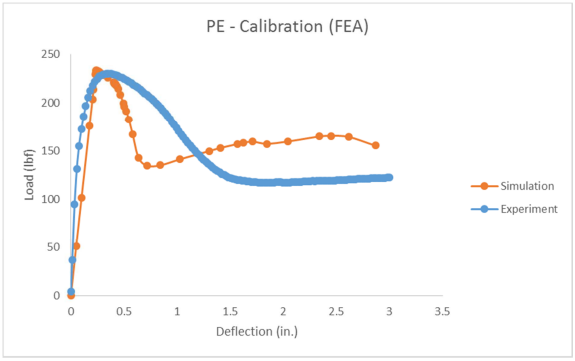

Figure 6.8: PE calibration curve from Polyumod (left) & curves from simulations (right)

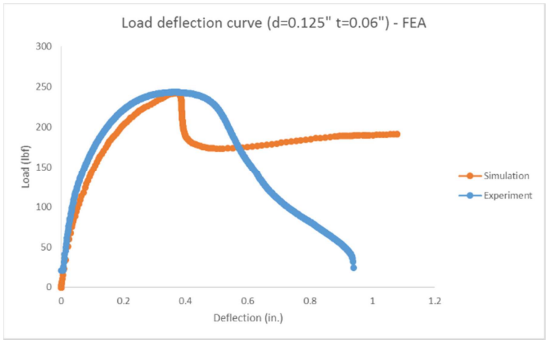

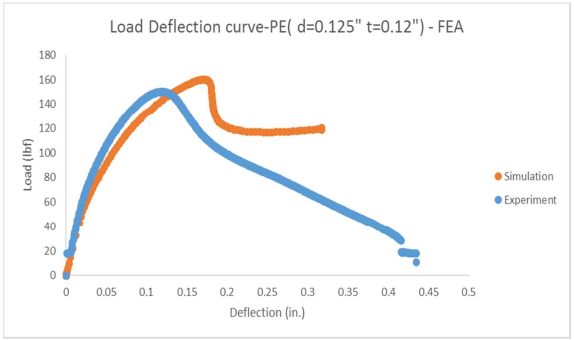

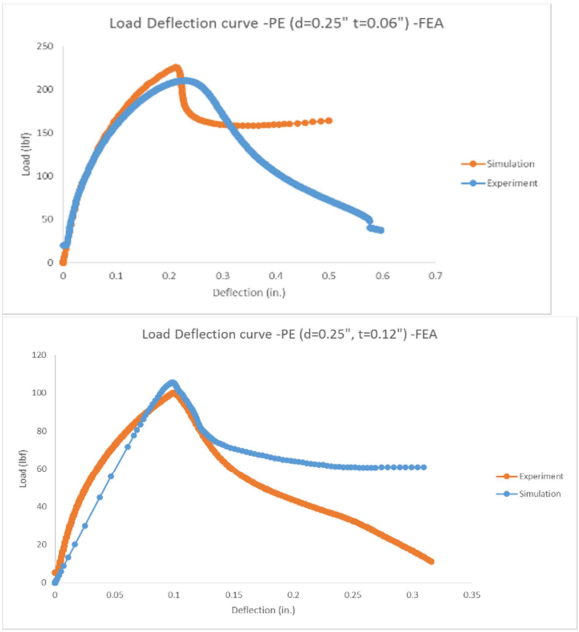

Figure 6.9: Load deflection curves comparing test & simulation results -FEA

As seen with PA-11, the results from the indentation testing for PE also were found to be similar to the smooth specimen results indicating minimal effect of indentation on the material properties. One the reasons for this observation is the degree of recovery of deformation induced by the indentor resulting in very minimal changes in the material properties when compared with the smooth specimen results.